The Thesis Committee for Amir Hossein Khalighi
Certifies that this is the approved version of the following thesis:

The Mitral Valve Computational Anatomy and Geometry Analysis

APPROVED BY
SUPERVISING COMMITTEE:

Supervisor:

Michael S. Sacks

Alison M. Pouch

The Mitral Valve Computational Anatomy and Geometry Analysis

by

Amir Hossein Khalighi, B.S.

Thesis

Presented to the Faculty of the Graduate School of

The University of Texas at Austin

in Partial Fulfillment

of the Requirements

for the Degree of

Master of Science in Engineering

The University of Texas at Austin

December 2015

Dedication

To my family and my friends

Acknowledgements

First, I would like to express my deepest gratitude to my supervisor, Professor Michael S. Sacks, for his support, patience, guidance, and encouragement throughout my studies. I was very privileged to have had the opportunity to work under his supervision and learn from his passion, profound knowledge, and meticulous observations. I could have not imagined having a better advisor.

I am also grateful to my second reader, Dr. Alison M. Pouch, for her invaluable input on my research, review of my thesis, and insightful comments. My very special thanks go to Dr. Andrew Drach for his mentorship, guidance, and patience. I will always be deeply indebted to him for introducing me to differential geometry, image processing, harmonic analysis, and stochastic modeling. I could not have imagined having a better mentor.

Great appreciation goes to our lab's collaborators on this project, the CFM Lab at Georgia Tech, for providing experimental data for our studies. Also, I would like to extend my gratitude to my labmates David Kamensky, Bruno Rego and Dr. Reza Avazmohammadi for their helpful discussions and shrewd comments on my work.

Special thanks to my friends Morteza Elahi Nargahi and Behzad Boroujerdian for their helpful thoughts on signal processing and optimization and more importantly their support. I also wish to thank all my friends and fellow labmates whom I have not named for their technical discussions and moral support.

Last but not the least, I would like to thank my family: my parents, Hassan and Maryam, and my cousin, Mehdi, for supporting me spiritually throughout my studies and my life in general.

Abstract

The Mitral Valve Computational Anatomy and Geometry Analysis

Amir Hossein Khalighi, M.S.E

The University of Texas at Austin, 2015

Supervisor: Michael S. Sacks

We present a novel methodology to characterize and quantify the Mitral Valve (MV) geometry and physical attributes in a multi-resolution framework. A multi-scale decomposition was implemented to model the MV geometry by using superquadric shape primitives and spectral reconstruction of the finer-scale geometric details. Superquadrics provide a basis to normalize the size and approximate a basic model of the MV geometry. The point-wise difference between the original geometry and the superquadric model denotes the finer-scale geometric details, which can be modeled as a scalar attribute for the MV model development. The additive decomposition of the basic MV geometry from geometric details (attributes) allows recovering the actual geometry by superposition of the superquadric approximation and the finer-details model. We implemented a lasso optimization algorithm to perform spectral analysis and develop the Fourier reconstruction of the geometric details. The spectral modeling enabled us to resample the geometric details or use spectral filters in order to adjust the spatial resolution in the model reconstruction. It also provides the basis to control the level of detail in the final model reconstruction by applying low-pass filters in the frequency domain. The higher-order

attributes such as internal fiber architecture can be integrated with the geometric models using the same framework. We applied our pipeline to create models of three ovine MVs based on computed-tomography 3D images with micrometer resolution. We were able to quantify the MV leaflet geometry, reconstruct models with custom level of geometric details, and develop medial representation of the MV leaflet structure. The results show that our methodology for geometry analysis provides a basis for assessing patient-specific geometries and facilitates developing population-averaged models. Ultimately, this approach allows building personalized image-based computational models for medical device design and surgical treatment simulations.

Table of Contents

List of Tables xi

List of Figures xii

Chapter 1: Introduction 1

Research Objectives 5

Thesis Outline 6

Chapter 2: Literature Review 7

Simplified Geometric Models 8

In vivo Geometric Models 9

Chapter 3: Materials and Methods 11

A. Data Acquisition 11

A.1. Materials and Methods 11

A.1.a. Heart Selection 11

A.1.b. Valve Preparation 12

A.1.c. Experimental Setup 13

A.1.d. Annulus adjustments 14

A.2. Micro-CT Imaging 15

A.2.a. Valve Instrumentation 15

A.2.b. Imaging Specifications 15

A.2.c. Systolic Configuration 16

A.2.d. Tissue Fixation 16

B. Data Processing 19

B.1. Image Denoising 19

B.2. Image Segmentation 20

B.3. Morphological Filtering 20

B.4. Geometry Construction 20

B.5. Morphological Labeling 21

C. Geometry Modeling 24

C.1. General Considerations 24

C.2. Multi-resolution Framework 25
C.3. Parametric Approximation (Superquadric Model).....26
C.3.a. Overview 26
C.3.b. Objective Function 28
C.3.c. Optimization Algorithm 30
C.3.d. Optimization Constraints.....32
C.4. Geometry Partitioning.....33
C.5. Modeling Geometric Details (Harmonic Reconstruction) 36
C.5.a. Geometry Decomposition.....36
C.5.b. Spectral Analysis.....42
C.6. Geometry Reconstruction.....51
C.7. Medial Representation.....52
C.7.a. Medial Surface.....53
C.7.b Thickness Field 53
Chapter 4: Results.....56
A. Overview.....56
B. Modeling Pipeline 56
B.1. Superquadric Models.....57
B.2. Attribute Modeling.....58
B.2.a. MV Geometry Partitioning.....58
B.2.b. Spectral Analysis.....60
B.2.c. Multi-resolution Reconstruction.....66
B.2.d. Medial Model 69

Chapter 5: Discussion and Conclusions....70

APPENDIX A – micro-CT Data-sets....72

APPENDIX B – Curvature Flow Filter....73

APPENDIX C – Morphological Filters....75

APPENDIX D - Superquadrics....76

Superquadric Fitting....77

APPENDIX E – Non-uniform Fourier Transform....79

Bibliography....81

List of Tables

Table 1: The annulus adjustment to simulate the healthy, Ischemic Mitral Regurgitation (IMR) and repaired valve by annuloplasty 15

Table 2: The soft tissue imaging adjustment 16

Table 3: Optimization setting in MATLAB for the trust-region-reflective algorithm 33

List of Figures

Figure 1: The view of the heart from the base with atria removed shows the MV's location and different structure compared to other heart valves (Schematic picture from the web).....1

Figure 2: The physiologic role of the MV is two-fold: (1) allowing oxygenated blood coming from the lungs to pass the left atrium and fill the left ventricle during cardiac diastole, (2) preventing the blood regurgitation back to the left atrium during cardiac systole, when the left ventricle contracts and pumps the blood to the entire body (Schematic picture from the web). 2

Figure 3: The Georgia Tech Cylindrical Left Heart Simulator (CLHS) was used to mimic the *in vivo* configuration of the MV inside the left ventricle of the heart. This experimental setup allows acquiring high-fidelity information on the MV geometry and mechanical behavior. 11

Figure 4: The adjustable annulus holder allows for the modification of the annular area and saddle height to simulate the healthy, dilated, and repaired MV configurations. The healthy state was acquired by preserving the normal configuration of the MV annulus. For the diseased state, the saddle height was reduced and the orifice was dilated. Finally, the annulus was tightened to simulate the restrictive MV annuloplasty procedure. ...13

Figure 5: (A) and (B) show our system to measure the pitch and yaw angles for the two rods attached to the papillary muscle heads. These rods were positioned for each valve according to the hemodynamic metrics of the MV output to simulate the healthy and remodeled left ventricle wall. 14

Figure 6: (A) and (B) show the difference in unfixed and fixed soft tissue imaging. Imaging the MV in vitro to acquire high-resolution geometry is non-trivial due to the tissue clamping on itself in the relaxed state. This requires simulating the normal open state of the valve dynamically and fixing the tissue under that condition. Then, the fine structure like the chordal tree branching and leaflet details would be fully resolved in the images.17

Figure 7: the soft tissue fixation in relaxed state. The open state of the MV was simulated and captured by a uniform flow of a fixative chemical in the CLHS. 18

Figure 8: (A) shows the 3-D segmented image of the MV mounted on the annulus holder. The fiducial markers placed on valve annulus enabled us to outline the annulus holder and remove it by Boolean operation to acquire the MV geometry (B). 22

Figure 9: The MV constituent parts are labeled. (A) shows the 3-D geometry of the entire MV with leaflets (red), chordae tendineae (blue), and papillary muscles (yellow). (B) shows the fiducial markers that we placed on the valve to track the displacement of the MV in order to validate biomechanical simulations. In this study, we focused on the study of MV leaflet structure shown in (C). We are currently working on the computational anatomy of chordae tendineae shown in (D). 23

Figure 10: (A) demonstrates a schematic representation of the MV apparatus (Adapted from (A. Carpentier, Adams, & Filsoufi, 2011). (B) Indicates that the general shape of the MV leaflets can be captured by a parametric surface reconstructed with a relatively small number of parameters. 25

Figure 11: The MV leaflet structure is topologically analogous to a torus. This means that the MV leaflet structure is considered to be from the family of geometrical objects that have one hole (genus-1). Panel (A) shows the 3-D view of the MV leaflets and a torus. Panel (B) shows the same shapes from top view. 27

Figure 12: the superquadric inside-outside function evaluated at an arbitrary point of the 3-D space is directly proportional to the r_0 / r_s ratio for that point. Consequently, the deviation of this function from 1 can be used in the design of an objective function to compute superquadric models, (Schematic adapted from (Jaklic et al., 2013)). 29

Figure 13: Curvature penalization allows capturing the MV hourglass geometry. (A) shows a representative superquadric model that would be computed without imposing the curvature criterion. (B) indicates how the curvature factor modifies the shape of a superquadric model. (C) represents a superquadric model analog to the MV leaflet geometry that is resolved by introducing curvature penalty. 30

Figure 14: The behavior of objective function with respect to shape parameters is demonstrated. The high density of iso-contours in plot (A) depicts the highly non-linear behavior of the objective function. Plot (B) shows the convex solution neighborhood in the optimization problem. 31

Figure 15: The objective function R is plotted versus the superquadric parameters a_1 and a_2, which denote the size of superquadric model in x and y directions respectively. This behavior suggests convexity of the objective function with respect to these parameters. 31

Figure 16: Curvature-based mesh partitioning for MV geometry cannot classify the mesh triangles into atrial and ventricular sides effectively. (A) shows the normalized mean curvature evaluated at the MV mesh vertices. In (B) we have shown the result of curvature-based mesh partitioning from two views. Although we expect to categorize the mesh triangles in atrial and ventricular groups, the curvature-based methods results in multiple clusters. This happens due to the fact that the MV surface has many bumps and creases that cause issues for defining decision boundaries to delineate the atrial and ventricular sides. 33

Figure 17: Iterative bisection algorithm to project a point cloud on the superquadric surface. Since we designed the projection algorithm using the superquadrics inside-outside function, the projection works well in spite of the non-convex superquadric surface. 35

Figure 18: the MV leaflet geometry, Panel (A), can be approximated with a superquadric surface fit shown in Panel (B). The superquadric fit provides an estimation of the MV size and shape. However, by definition, it cannot capture the regional thickness and features of the MV leaflet surface.37

Figure 19: In our framework, we considered the superquadric model to be a first-order approximation of the 3-D MV geometry. For the purpose of most biomechanical simulations the superquadric surface fit can be used, shown in (B), to build a 3-D basic model of the input geometry, shown in (A). 37

Figure 20: the superquadric approximation of the MV leaflets structure provides a basic parametric model for the valve geometry. (A) shows a representative MV geometry and a superquadric model that approximates the MV shape; (B) to (E) illustrate generating a cross sectional view of the MV leaflet structure and its superquadric model. (F) indicates the fact that a superquadric model only provides a basic approximation of the MV geometry. It also illustrates the degree to which the 3-D geometry of the MV might be different from its superquadric model. 38

Figure 21: to capture the MV geometric details, we evaluated the deviation of MV atrial and ventricular sides from the computed superquadric model of the MV leaflets. White and yellow arrows refer to the normal distance of the MV atrial and ventricular sides from the superquadric model respectively. To reconstruct the MV geometry with high accuracy, we modeled these normal distances as scalar fields defined on the parametric domain of the superquadric surface. 39

Figure 22: the procedure to define the domain of the MV geometric details is illustrated. The MV surface features can be quantified as deviation fields that consist of the L_2 distance between the input geometry and the superquadric model. Plot (A) illustrates the location of our cross sectional view. Plots (B) shows a highlighted region on the input mesh. The same projection of this highlighted region on the superquadric model is shown in (C). The point-wise distance between the input mesh and the projected one denotes the geometric details of the MV surface. 40

Figure 23: (A-B) Representative MV mesh projected on the superquadric model, with periodic boundary highlighted in blue. (C) Plot of the MV mesh projected on its parametric space. This mapping 3-D Cartesian space to the 2-D parametric domain of the superquadrics allowed us to reconstruct the geometric details of the MV surface in a way that can be integrated with the superquadric model. The MV geometry occupies a narrow region in the parametric domain so it has been shown on a section of the space *(-π/4<η<0).* 41

Figure 24, the irregular domain for the MV geometric details is illustrated from 2 views. To model the MV surface bumps and creases, we were required to reconstruct the pointwise distance between the input geometry and the superquadric model. However, since the input geometry is defined as a triangulated surface, the distance maps denoting the atrial and ventricular surface details are defined on domains with non-uniform structures.44

Figure 25: The Gaussian gridding approach for NUFFT interpolates the data on a super-sampled Cartesian grid shown in (A). For the MV attributes this results in zero-padding the data in subdomains of the parametric space where the MV domain is not defined, shown as grey in (B). Applying FFT for computing the Fourier transform of the interpolated function fails due to the discontinuity of data on the MV irregular boundaries, highlighted in (B). 46

Figure 26: In Fourier reconstruction, we modeled the effect of MV boundaries as a mask shown here, multiplied by an underlying function that is defined over the entire parametric domain of superquadrics and denotes the MV geometric details. This function when sampled inside the MV parametric domain recovers the geometric details of the MV surface. 48

Figure 27: Our iterative approach for sparse spectral analysis is described. The algorithm requires setting a threshold for filtering the noise that is an artifact of irregular boundaries. The threshold was chosen empirically to be 1×10^{-4} for all valves.....50

Figure 28: The discrepancy between the medial surface and the superquadric model is shown. Plot (A) represents a cross sectional view of a MV geometry modeled by a superquadric surface. This cross section is shown in normal view in plot (B). The spectral analysis in our framework allows evaluating the medial surface based on the superquadric model.....52

Figure 29: The medial surface location can be approximated by averaging the distance of atrial and ventricular surfaces from the superquadric model. 53

Figure 30: The MV leaflet local thickness can be defined as the radius of the spheres that are centered at the medial surface and tangent to the atrial and ventricular boundaries.....54

Figure 31: The normal to the superquadric surface is not necessarily in the same direction as the normal to the medial surface, shown as angle θ. The thickness field computed by using spectral reconstruction of the geometric details needs to be projected on the normal to the medial surface. This is done by multiplying the reconstructed thickness fields by $cos(\theta)$ that is evaluated pointwise on the medial surface. 55

Figure 32 Computed superquadrics for three MVs are shown from two views in the Panels (A) and (B). For all the valves, the computed superquadric models are relatively similar and belong to the same family of superquadric shapes, shown in Panel (C). 57

Figure 33: Mesh partitioning results to extract the atrial (beige) and ventricular (maroon) side surfaces are shown. 59

Figure 34: The annulus and free edge for 3 valves are shown as blues curves from two views. Geometrically, these curves can be sued to approximate the boundaries of the MV medial surface. 60

Figure 35: The regions depicted by black arrows where the valve surface has folded on itself are not recoverable by our approach. Plot (A) shows one of our studied valves that has a few folds. In Plot (B) we have shown the region that our methodology considers as high-frequency noise and filters out in the spectral analysis. 61

Figure 36: The two mappings required to model the geometric details of the MV leaflet is represented. The ventricular side is represented on the left and atrial on the right. The surface mesh (A) is normally projected on the superquadric fit to acquire (B). Shown in (C), the signed L_2 distance between these two meshes in (A) and (B) indicates the deviation of MV actual surface from the superquadric model. Then, the deviation fields evaluated on 3D Cartesian meshes are projected on the superquadric parametric domain as shown in (D). 62

Figure 37: The reconstruction of MV geometric details for one of the studied valves, is demonstrated. Panel (A) shows the reconstruction of ventricular and atrial sides on the left and right figures respectively. The reconstruction error for both sides is illustrated in Panel (B) in the same order. It should be noted that the reconstruction error is localized in the regions where the MV surface is folded on itself.....64

Figure 38: The reconstruction MV atrial and ventricular sides with the geometric details is illustrated. (A) shows the MV geometry input in the pipeline and its superquadric fit. In (B) the superquadric model is enriched with the geometric details to recover the fine features of the MV surface. Plot (C) shows the unique extension of the geometric details to the entire parametric domain which need to be restricted to the physical domain to recover the actual MV geometry.....65

Figure 39: The spectral modeling, by definition, reconstructs the geometric details on the entire superquadric surface as shown in (A). Our parametric representation provides an explicit equation to reconstruct MV surfaces. Thus, we imposed the annulus and free edge, shown in (B) as boundaries for the parametric reconstruction. Plot (C) shows the reconstruction of MV atrial and ventricular surfaces. The result (C) shows the surfaces separate since the spectral analysis filters out the annulus and free edge regions due to their high curvature. To recover a closed representation NURBS parching can be used to stitch the two sides smoothly. 66

Figure 40: the spectral representation of the MV geometric details for the ventricular side for one of the studied MVs is shown in decibel. Plot (A) illustrates that the frequency spectrum is sparse and mostly concentrated at low frequencies. The horizontal axis (n) represents the frequencies along ω and the vertical axis (m) denotes the frequencies along η directions, equation (6). The low-frequency ensemble which contains more than 99% of the power spectrum density is shown in plot (B). This result indicates that we can reconstruct the MV geometric details using a relatively small number of frequencies.....67

Figure 41: The results of multi-resolution reconstruction are shown for three MVs. Panel (A) shows the superquadric fits for three valves. This basic model was then morphed by adding the DC frequency to reconstruct the atrial and ventricular surfaces in (B). Integrating more frequencies in the reconstruction recovers more geometric details as shown in (C) and (D). The original geometry that is input to our pipeline is shown in (E). The hierarchical reconstruction performed by tuning the cut-off frequency in the spectral reconstruction of attributes can allow controlling the level of detail in attribute-rich model development. 68

Figure 42: The medial representation of the MV leaflet structure is shown. (A) shows the reconstruction of the atrial and ventricular sides on the superquadrics parametric domain. In (B) these surfaces are averaged to acquire the location of medial surface. The complete medial representation of the MV restricted to the physical boundaries and with pointwise scalar fields is shown in (C). The thickness fields is an attribute of the MV physical structure that is essential for using shell models for finite element simulations of the MV biomechanical behavior. 69

Figure 43: The standard objective function used to fit superquadric models fails to fit an acceptable model to the MV geometry. This is due to the fact that this objective function finds the closest model to the input geometry with elliptical topology. The MV geometry, however, is analogous to an hourglass shape. 78

Chapter 1: Introduction

The Mitral Valve (MV) is the bi-leaflet heart valve separating the left atrium and left ventricle that regulates blood flow direction during cardiac cycles. The MV complex is comprised of anterior and posterior leaflets, annulus, chordae tendineae, and papillary muscles (PM). The geometry of MV leaflets is unique as it is the only heart valve with the natural dual-flap structure, (Figure 1).

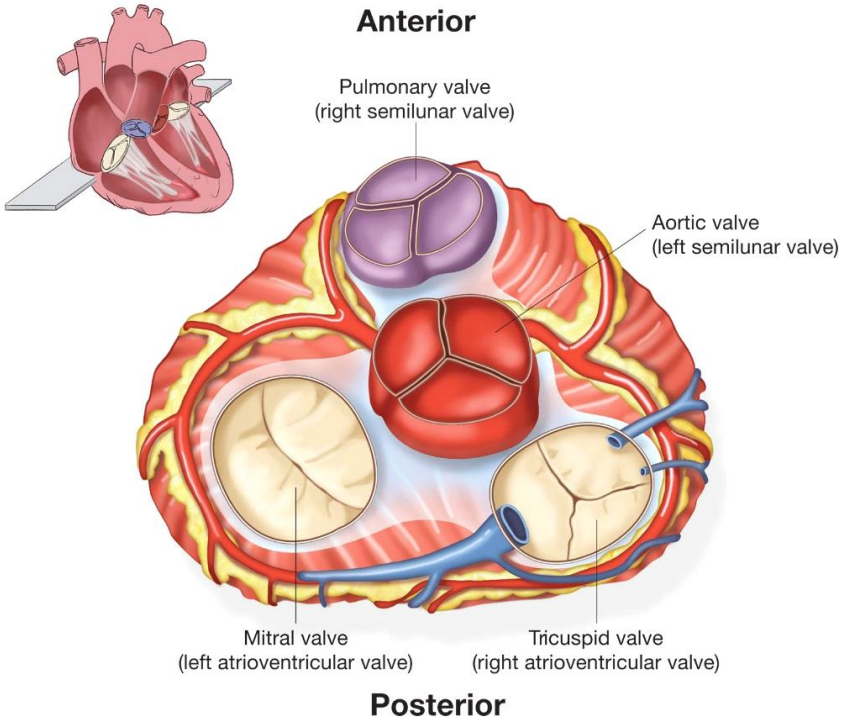

Figure 1: The view of the heart from the base with atria removed shows the MV's location and different structure compared to other heart valves (Schematic picture from the web)

The physiological role of the MV is highly dependent on the interconnected relation of the MV constituent parts (Madesis et al., 2014). The MV leaflets are tethered to the left ventricle through chordal structure, which protrude from two PMs on the ventricular

endocardium and insert into the leaflets at multiple locations. The geometry of the MV has a critical impact on the valve's competence. The MV leaflets cover the left atrioventricular orifice during systole to prevent regurgitation of oxygenated blood back to the left atrium. During the diastole, the leaflets relax and allow the blood coming back from the lungs and through the atrium to fill the left ventricular chamber (Figure 2). Deviations from this required behavior lead to mild-to-severe valvular insufficiencies and even further complications like stroke (Sutton & Weyman, 2002).

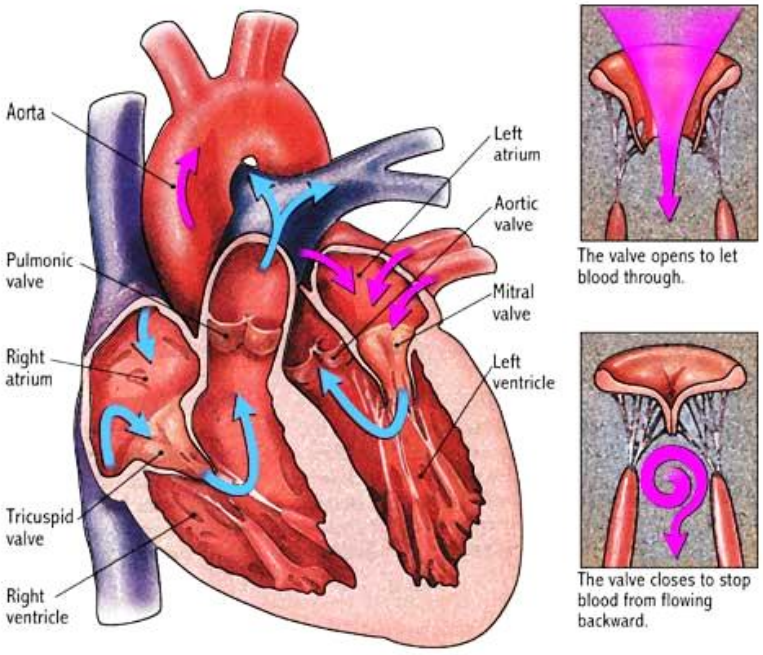

Figure 2: The physiologic role of the MV is two-fold: (1) allowing oxygenated blood coming from the lungs to pass the left atrium and fill the left ventricle during cardiac diastole, (2) preventing the blood regurgitation back to the left atrium during cardiac systole, when the left ventricle contracts and pumps the blood to the entire body (Schematic picture from the web).

Most MV complications are characterized by deviations from the native shape and non-homeostatic configurations of the MV with respect to the heart wall (Schueler et al., 2014), (Neema, 2013), (Benjamin, Smith, & Grayburn, 2014). Mitral Valve Regurgitation

(MVR) is the most prevalent valvular heart disease, which some predict to become an epidemic issue as the population grows and ages (d'Arcy, Prendergast, Chambers, Ray, & Bridgewater, 2011) . MVR occurs when the valve leaflets fail to fully cover the MV orifice area and blood leaks to the left atrium during systole, (Pedrazzini, Faletra, Vassalli, Demertzis, & Moccetti, 2010). The causes of MVR can be either primary (myxomatous degeneration and rheumatic fever) or secondary (ischemic left ventricular remodeling), (Enriquez-Sarano, Akins, & Vahanian, 2009).

There is still no definitely effective treatment to fix a leaking MV, with the heart valve replacement and repair being the common approaches (Kheradvar et al., 2015), (Acker et al., 2014). Mitral annuloplasty is currently the most-practiced MV repair technique, which is based on restoring the optimal size and shape of the MV annulus (A. F. Carpentier et al., 1995). In the annuloplasty procedure, a ring is sutured on the MV orifice near the MV annulus region to shrink the orifice size so that the s coapt completely. However, in spite of intense research on this problem, there is still no clear evidence on the optimal annuloplasty procedure (Bothe, Miller, & Doenst, 2013). Furthermore, patient-specific MV geometry has been shown to affect the repair durability and effectiveness (Salgo et al., 2002), while repair technique planning remain mostly qualitative.

It is believed that the complex MV structure and tissue remodeling play a significant role on the valvular response to repair (Flameng, Meuris, Herijgers, & Herregods, 2008). Isolating the effect of each factor to study the valvular response is not feasible in the *in vitro* and animal studies. On the other hand, computational simulations of heart valve behavior have proven to be promising tools to enhance our understanding of the valvular mechanisms and response to pathological alterations (Chandran, 2010). However, due to the complexity of MV behavior, the computational models are still struggling to account for all the underlying features that impact the MV behavior. The

state-of-the-art MV computational models suffer from three major approximations that affect the fidelity of simulations:

First, most performed MV studies have relied on suboptimally reconstructed or simplified geometries (Hammer, Perrin, Pedro, & Howe, 2008), (V. Prot, Skallerud, Sommer, & Holzapfel, 2010). This problem is generally inevitable since even most advanced imaging techniques cannot fully resolve the complete MV apparatus *in vivo*. Consequently, many MV computational simulations have relied on post-mortem *in vitro* measurements to build geometric models of the MV (K. S. Kunzelman et al., 1993), (V Prot, R Haaverstad, & B Skallerud, 2009), (Khalighi et al., 2015), (Drach et al., 2015). However, excising the valve from the body causes deviations in the shape and structure, which are mostly intractable and further affect the reliability of simulations (Amini et al., 2012). Moreover, postmortem data acquisition is obviously impractical for developing personalized human models and performing patient-specific simulations for treatment planning.

Secondly, it has been shown that the MV multi-layered structure and fiber architecture play a significant role in the valvular mechanical behavior (Lee et al., 2015). However, incorporating this information in the modeling is by no means trivial. The data on geometry, material properties and internal structure are collected using different modalities and assimilating them is prone to mapping degeneracies and interpolation errors. Thus, patient-specific modeling requires new approaches to faithfully predict the structural information and material properties of the heart valve tissue.

Finally, the MV behavior and response to repair is driven by physical and physiological phenomena occurring from organ-level to cellular-level scales. The current MV computational models are not capable of effectively linking the cellular level undertakings and the organ level response. Multi-scale modeling of the MV to account for

tissue remodeling requires computational models that facilitate incorporating the MV structural attributes from various scales. However, the current geometric models of the MV used for finite element simulations cannot effectively link different scales of the MV structure.

Therefore, there is an urgent need for the development of computational models of the MV geometry that provide high anatomical accuracy, structural information, and connection to the valvular physiology. Such computational models can provide the means to perform high-fidelity simulations for the population as well personalized modeling. Furthermore, structurally-informed models of the MV facilitate the simulation of diseased states and thus can lead to new treatment design.

In the current study we have developed a pipeline to quantitatively characterize the MV geometry, build personalized models with adjustable level of detail, and integrate the MV geometry with its structural attributes. Moreover, our framework allows the study of inter-subject variations and facilitates developing a population-averaged model by providing a correspondence between MVs. To the best of our knowledge, this is the first rigorous study on the development of attribute-rich computational models of the MV.

RESEARCH OBJECTIVES

The main objective of the current study was to develop a pipeline to analyze the MV leaflet geometry and establish the framework to incorporate attributes into the MV computational models. In this thesis document, we have extensively reviewed our methodology and discussed our results for the study of 3 ovine MVs. The notable research objectives are summarized as below:

1. Acquire the MV geometry with high-fidelity in an *in vitro* setup

2. Develop an image processing pipeline to analyze micro-CT images of the MV
3. Co-register different MV geometries with respect to anatomical landmarks such as Anterolateral and Posteromedial commissures
4. Establish a multi-resolution framework to the study the MV geometry and physical attributes
5. Develop an algorithm to incorporate the MV structural attributes into computational models with high fidelity
6. Build a medial representation of the MV geometry suitable for finite element modeling

THESIS OUTLINE

This document is organized in five chapters following the format of an extended journal publication. After the introduction, the literature on the MV geometric models is reviewed. In the third chapter, we have thoroughly described our methodology to acquire experimental data, build geometrical representations of the MV, and analyze the MV geometry using our novel multi-resolution framework. In chapter four, the results of our pipeline implementation and analysis of three datasets are provided. In the fifth and final chapter, we have summarized the conclusions of our study and some recommendations for future research directions.

Chapter 2: Literature Review

In this chapter we review the geometric models used to perform computational simulations of the MV biomechanical behavior. The information required for the *in silico* study of the MV as mechanical system has three general components: (1) a constitutive relation that relates the kinematics and dynamics, (2) a physical domain with defined material properties, and (3) proper boundary conditions that drive the response. All these three factors greatly impact the predicative power of computational methods to simulate the behavior of a mechanical system. However, we believe that the MV geometry has been overlooked in the previous studies in spite of its fundamental role and impact on the modeling.

The reconstruction and modeling of MV geometry is generally obtained by imaging the valve to acquire precise information about its complex morphology. The preferred environment for collecting these images is *in vivo*, since it provides the most physiologically realistic information and can be leveraged to develop patient-specific models. However, the fine geometric features, namely the MV chordal structure, are only resolvable through *in vitro* imaging. Three main imaging modalities used to acquire MV structure are (1) ultrasound, (2) Magnetic Resonance (MR), and (3) Computed Tomography (CT). Here, we discuss the geometric models of the MV that have been developed in the previous studies.

We classify the geometric models used in the previous works on MV computational modeling in two general groups: simplified models, *in vivo* models. For simplified models, a combination of *in vitro* measurements on post-mortem tissue and simple measurements on the *in vivo* images have been used to develop a simplified geometric model. The *in vivo* models has relied mostly on the geometric information extracted from the clinical medical

images to better capture the actual geometry of the MV inside the heart. Most recently, the atlas-based models of the MV based on *in vivo* ultrasound imaging have been extensively pursued due to the improved reliability and efficiency. In the rest of this chapter we have reviewed some notable examples of each class of MV geometric models.

SIMPLIFIED GEOMETRIC MODELS

Kunzelman et al. (K. Kunzelman et al., 1993) developed the first 3D finite element model of the MV. They included the regional thickness variations, collagen fiber architecture, and anisotropic material properties in their computational model. In terms of geometry, they performed their simulation on a simple symmetric model that was developed based on *in vitro* physical measurements.

Prot et al. (V. Prot, R. Haaverstad, & B. Skallerud, 2009) (V Prot & Skallerud, 2009) performed measurements on post-mortem porcine tissue to acquire geometric dimensions of the MV. They assumed the MV leaflets to be planar with constant unit thickness through the entire structure. To simplify their model, they excluded the commissural regions from the leaflet structure and considered the MV annulus to be flat and symmetric.

Votta et al. (Votta et al., 2008) extracted the annular profile from ultrasound images and included the unsymmetrical saddle shape of the annulus. To construct the leaflet structure, they extruded the leaflet profile along axis normal to annular plane and then tilted the generated surface to acquire a surface model that qualitatively matches the echocardiography images. To build their shell model for simulation, they assumed the anterior and posterior leaflets to have the constant thickness of 1.32mm and 1.26mm.

Maisano et al. (Maisano et al., 2005) used the same in vitro measurements reported in the litrature (Kunzelman, Cochran, Verrier, & Eberhart, 1994) to develop a geometric representation of the MV. They assumed a flat circular profile for the annulus and generated a symmetric shape for the MV leaflets to simulate the healthy state of the MV. Then, they modified their dimensions and repeated the simulations on D-shaped and dog-bone-shaped annular profiles to simulate the surgically modified MVs. They considered the uniform thickness of 0.8 mm for all of the cases that they studied.

Skallerud et al. (Skallerud, Prot, & Nordrum, 2011) used a 3D ultrasound imaging technique to measure the shape of the MV annulus and extracted the leaflet geometry from post-mortem tissue. They simplified the annulus geometry as a non-planar ellipse, which had a relatively small eccentricity according to their in vivo measurements. They idealized the leaflet geometry with symmetric outlines and assumed constant unit thickness for the entire leaflet structure.

IN VIVO GEOMETRIC MODELS

Lim et al. (Lim, Yeo, & Duran, 2005) used CAD software packages to construct a MV geometric model based on the end-diastole coordinates of 12 transceiver crystals implanted on the MV annulus. For the leaflet structure, they fitted a spline surface to the annulus and free edge crystals. They assumed a constant average thickness of 1.26 mm for the leaflet in spite of the variations in thickness from 0.5 mm in the leaflet belly to 2 mm in the trigons. They used their model to simulate the stress distributions in the MV leaflets under physiologic loading.

Stevanella et al. (Stevanella et al., 2011) developed a patient-specific model of the MV based on end-diastolic images acquired using cardiac magnetic resonance. They fitted

spline curves to the outlines of the annulus and free edges in these images. Then, they used these boundary curves to define the leaflet surface. For the thickness, they applied a regional thickness map based on the values acquired from post mortem tissue reported in the literature. Using this geometry modeling method, finite element models were developed for a healthy and a regurgitant MV to study their mechanistic response.

Wang and Sun (Wang & Sun, 2013) based their analysis on the patient-specific multi-slice CT images to capture the full MV structure. They extracted a discretized representation of the MV leaflets with regional thickness values using image segmentation. This enabled them to develop an anatomically consistent leaflet structure as well as a kidney-shaped annulus with non-zero out-of-plane saddle height for their studies.

Choi et al. (A. Choi, Rim, Mun, & Kim, 2014) developed a patient-specific model of a MV with annular dilation based on 3D Trans-Esophageal Echocardiography (TEE) imaging. After image segmentation, they fitted NURBS surfaces to the 3D leaflet structure and annulus geometry. They simulated the MV ring annuloplasty procedure by imposing an annuloplasty ring on their model and modifying the geometry.

Pouch et al. (Pouch, Yushkevich, et al., 2012) developed a deformable template for the MV leaflet structure that allows semi-automatic segmentation of *in vivo* TEE images to acquire MV geometric models. In another study, Pouch and colleagues (Pouch, Xu, et al., 2012) demonstrated the capability of their methodology to build patient-specific geometric representations of the MV, suitable for finite element analysis, based on medial representation of the MV. Witschey et al. (Witschey et al., 2014) used the same framework to successfully develop quantitative virtual models of the MV under normal, ischemic, and myxomatous conditions to potentially guide surgical therapy.

Chapter 3: Materials and Methods

A. Data Acquisition

A.1. Materials and Methods

We used *in vitro* micro-computed tomography (micro-CT) to provide high-resolution 3D images of ovine Mitral Valve (MV) geometry. The following details the process and technique used to obtain the 3D images from micro-CT using the Georgia Tech Cylindrical Left Heart Simulator (CLHS) (Rabbah, Saikrishnan, & Yoganathan, 2013), (Figure 3)

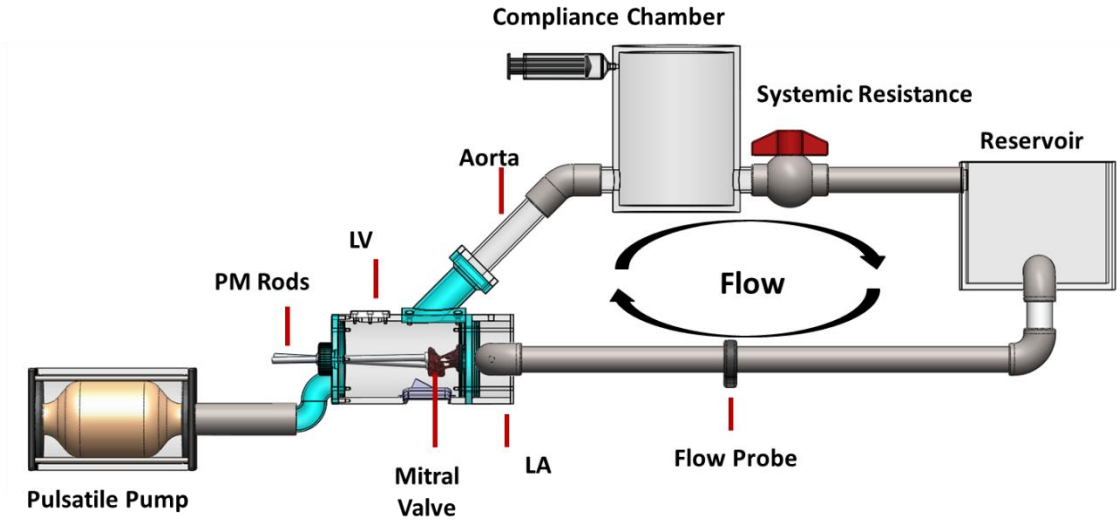

Figure 3: The Georgia Tech Cylindrical Left Heart Simulator (CLHS) was used to mimic the *in vivo* configuration of the MV inside the left ventricle of the heart. This experimental setup allows acquiring high-fidelity information on the MV geometry and mechanical behavior.

A.1.a. Heart Selection

We procured fresh (never frozen) hybrid Dorset ovine hearts from an abattoir (Superior Farms, California). MVs were sized using a clinical annular sizer set, and only

valves with commissure-to-commissure size of 26 *mm* were used for this study, as valves of this size were compatible with the loop hardware. Additionally, we inspected the papillary muscles (PMs) and the valves with either type I or type II PMs (Berdajs, Lajos, & Turina, 2005) were used. As the final criterion, we used valves with an anterior leaflet length of 20±1mm. We then carefully excised the MV and the sub-valvular apparatus from the heart.

A.1.b. Valve Preparation

After excision, the mitral annulus was sutured to a rigid plate using a ford interlocking stitch just above the natural hinge line. Physiological landmarks (left and right trigone, anterior annular horn, A2/P2 line) were aligned with their corresponding geometric landmarks on the annular plate. The rigid plate separates the atrial and ventricular chambers of the CLHS (Figure 4), and has an idealized annular orifice to which each valve was sutured. Then, we affixed the PMs to two rods, mounted to ball in socket joints to control their position.

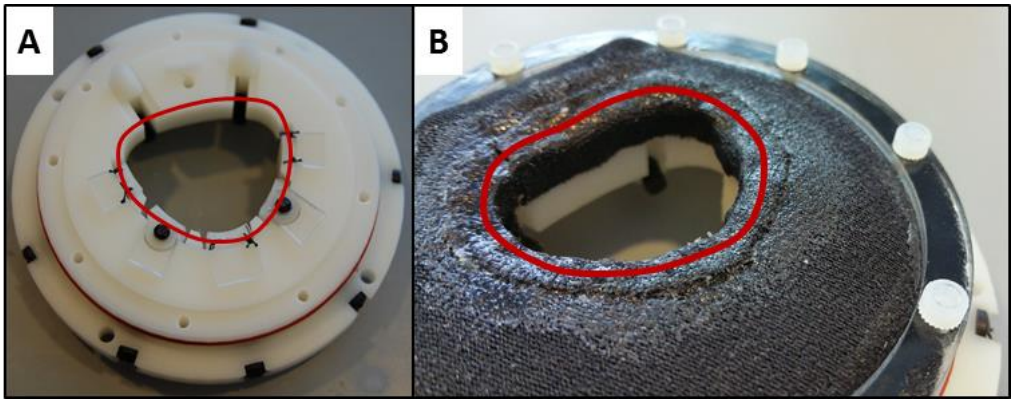

Figure 4: The adjustable annulus holder allows for the modification of the annular area and saddle height to simulate the healthy, dilated, and repaired MV configurations. The healthy state was acquired by preserving the normal configuration of the MV annulus. For the diseased state, the saddle height was reduced and the orifice was dilated. Finally, the annulus was tightened to simulate the restrictive MV annuloplasty procedure.

A.1.c. Experimental Setup

After mounting the MV to the CLHS, we inserted the chamber into a pulse duplicator system, which uses a pulsatile pump and a series of lumped compliance and resistance elements to mimic physiological pressure and flow waveforms. The pump timing and data acquisition was controlled with a custom LabVIEW control interface (National Instruments, TX, USA). Standard hemodynamics were then reached in the system (5 liters per minute, heart rate of 70 beats per minute, peak transvalvular pressure of 120 mmHg). We used a clinical echocardiography unit (Philips Healthcare, MA, USA) to monitor clinically relevant healthy mitral closure parameters while PMs were adjusted to their control positions. We adjusted the PMs to achieve minimal regurgitation, eliminate leaflet tenting or prolapse, minimize chordal tethering, and ensured that the anterior leaflet occupied two thirds of the A2/P2 distance. These locations were recorded by a custom system to measure the pitch, yaw and radius of each PM controlling rod (Figure 5). Such

control over PM positions enables us to simulate LV remodeling in secondary MR by relocating PMs.

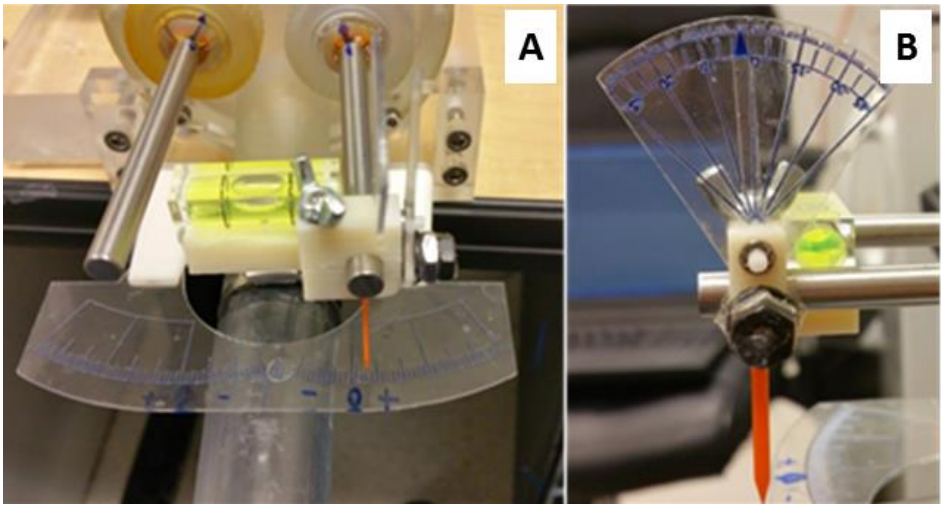

Figure 5: (A) and (B) show our system to measure the pitch and yaw angles for the two rods attached to the papillary muscle heads. These rods were positioned for each valve according to the hemodynamic metrics of the MV output to simulate the healthy and remodeled left ventricle wall.

A.1.d. Annulus adjustments

We studied the valve under healthy, diseased, and surgically modified configurations by adjusting the saddle shape of the annulus to simulate each configuration (Table 1). To control the annulus shape, we designed and implemented a custom adjustable plate to replicate the changes in annular geometry observed in chronic ischemic LV remodeling. Shown in Figure 4, the posterior aspect of the annulus is split into five segments, which move radially in and out of the mitral orifice on plastic worm screws. This replicates the annular distension and dilatation seen in ischemic LV remodeling (Gorman, Jackson, Enomoto, & Gorman, 2004), (Gorman III, Ryan, & Gorman, 2006), (Vergnat et al., 2011). Additionally, the anterior aspect of the annulus is fabricated from flexible PETG

sheet that is fixed at the anterior horn. Wedges at either commissure travel on worm screws, which we adjust to simulate the geometry of the MV under different conditions.

Table 1: The annulus adjustment to simulate the healthy, Ischemic Mitral Regurgitation (IMR) and repaired valve by annuloplasty

Geometric Metrics	Healthy	IMR	Restrictive Annuloplasty
Anterior-Posterior distance (mm)	24 mm	30 mm	24 mm
Inter-Commissural distance (mm)	30 mm	33 mm	30 mm
Annular height-commissural width ratio	15%	0% (flat)	0% (flat)

A.2. Micro-CT Imaging

A.2.a. Valve Instrumentation

Prior to micro-CT imaging, we attached sand and clay beads on the valve leaflet surface in a dense grid layout. This technique has been previously described (Pierce et al., 2015), and allows for deformation tracking of the MV across micro-CT scans under different loading configurations. Moreover, these markers can be used to validate the biomechanical simulations of the valve behavior (Lee et al., 2015).

A.2.b. Imaging Specifications

To acquire high-resolution MV images, we used a Siemens Inveon micro-CT scanner (Siemens Medical Solutions USA Inc., PA, USA), with settings optimized for soft tissue imaging (Table 2), We collected ten separate data sets, but then selected the best five ones for our studies [APPENDIX A]. The Imaging time per valve was approximately 7

minutes; the resulting volumes were comprised of 43.29-micron voxels with isotropic resolution.

Table 2: The soft tissue imaging adjustment

Voltage	Current	Integration Time	Projection Count
80 *kV*	500 μA	650 *ms*	180 *Radial*

A.2.c. Systolic Configuration

Directly following the application of beads, we imaged the MV under simulated low and high loading. We used a compressor with an in-line humidifier to apply static pressure to the closed MV, mimicking a systolic configuration. Humidity in the CLHS chamber was kept at roughly 100% during scanning. Two systolic scans at 30 mmHg and 100mmHg were taken of the MV in each geometric configuration (healthy, diseased, and repaired), yielding a total of six systolic micro-CT scans per valve.

A.2.d. Tissue Fixation

It is significantly challenging to capture the diastolic geometry since diastole is a naturally dynamic state. We realized that the small features and details in the chordal tree would bunch together when the chamber was drained of saline during the micro-CT imaging. This can be attributed to the low stiffness of the MV leaflet and chordal tissue. Additionally, the thin sections of leaflet would fold in on themselves, yielding a diastolic

image where the leaflet area was under-represented, and the chordal details were missing (Figure 6).

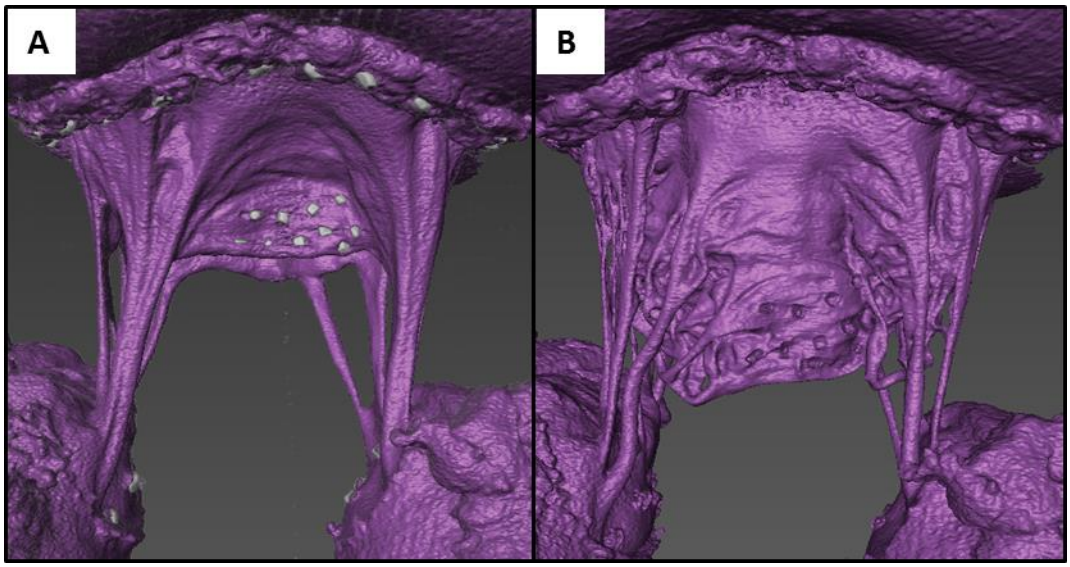

Figure 6: (A) and (B) show the difference in unfixed and fixed soft tissue imaging. Imaging the MV in vitro to acquire high-resolution geometry is non-trivial due to the tissue clamping on itself in the relaxed state. This requires simulating the normal open state of the valve dynamically and fixing the tissue under that condition. Then, the fine structure like the chordal tree branching and leaflet details would be fully resolved in the images.

To counteract the cohesive and adhesive forces of residual water on the MV, we used the stiffening effect of glutaraldehyde to fix the tissue (Vesely & Boughner, 1989). After imaging the MV in its systolic state (with fresh tissue), we dripped a solution of 0.5% glutaraldehyde over the valve for two hours in a vertical fixation loop (Figure 7). This simultaneously unfurls and spreads the valve features while stiffening the tissue for the final diastolic imaging stage. After performing fixation for two hours, we imaged the MV in the unloaded state under the healthy, diseased and repaired configurations.

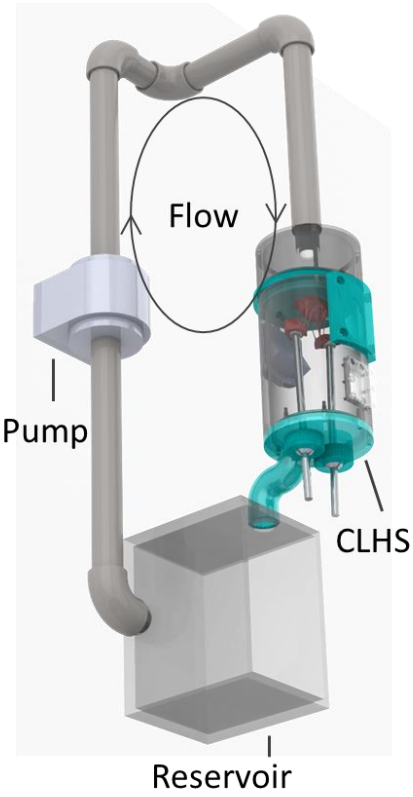

Figure 7: the soft tissue fixation in relaxed state. The open state of the MV was simulated and captured by a uniform flow of a fixative chemical in the CLHS.

B. DATA PROCESSING

We loaded the DICOM images into the ScanIP software suite (Simpleware Ltd., Exeter, UK) to process the images and create geometric representations. Each DICOM dataset consists of 3 stacks of 2D images, which are co-registered orthogonally. Each 3D image is a 32-bit gray-scale map that correlates to the X-ray absorption values as it traces through the tissue. The voxel size is 43.29 micron and the dataset contains 1024 images in each direction. Prior to image processing, we examined each 3D image stack in the ScanIP software suite to ensure that the dataset is usable, (APPENDIX A). Next, we filtered the images and segmented the structure from the image background. We then used the morphological filters to improve the segmentation results and finally create 3-D mesh representations of the valve geometry. These steps are described in the rest of this section.

B.1. Image Denoising

We used a two-step procedure to filter artifacts polluting the images, using a median filter and a non-linear anisotropic diffusion based filter. First, we applied an isotropic median filter to remove the salt-and-pepper noise. Next, we applied an anisotropic diffusion filter to treat the signal diffraction and attenuation artifacts (You, Xu, Tannenbaum, & Kaveh, 1996). Diffusion-based filters redistribute the intensity values inside the domain of an image by solving a transient diffusion equation (Weickert, 1998). We selected the curvature flow type from the diffusion-based filters described in the literature (Malladi & Sethian, 1995). [We discuss this choice in more detail in APPENDIX B.] Applying a median and a curvature-flow filter successively, we achieved an image quality sufficient for image segmentation.

B.2. Image Segmentation

We used a thresholding method to segment the filtered images. In this method, two limit values are chosen to define the intensity interval that corresponds to the structure of interest in an image. Our desired structures in each image were the valve tissue and the physical markers. To guide the thresholding procedure, we used multiple sample locations and the histogram of image intensity values. The output of the segmentation procedure is a binary map that denotes the desired structure by one and unoccupied regions by zero. These maps are often called label fields or binary masks in the image processing literature (Sezgin, 2004). Using the thresholding method to identify valve tissue and extract the markers, we constructed two 3-D binary masks per valve.

B.3. Morphological Filtering

Even though we denoised the images prior to segmentation, the binary masks were still polluted in some regions. The main polluting artifacts are due to (1) instrumenting the valve with sand/clay markers and (2) imaging the valve in an *in vitro* setup. We have discussed the morphological filtering procedure we applied to enhance the quality of binary mask in APPENDIX C. By finishing this step, we acquired the 3-D binary-field representations suitable for geometric analysis.

B.4. Geometry Construction

To model the valve surface geometry, we required a boundary representation (B-rep) of the valve in place of 3-D binary masks. The binary field or voxel representation consists of a classification function from 3-D Cartesian space to {0,1}. This type of shape representation is simple and efficient in terms of required memory. Nevertheless, it lacks

any information on the topology or boundary locations. To convert volumetric binary field representations to polygonal meshes, marching cubes is a commonly used algorithm (Lorensen & Cline, 1987). We used the marching cube algorithm implemented in the ScanIP software suite to create a triangulated surface representation of the geometry for each valve. The mesh files were then imported in Zbrush sculpting software (Pixologic Inc., CA, USA) for manual morphological labeling.

B.5. Morphological Labeling

We labeled the geometric representation of each valve to extract the leaflet structure, chordae tendineae, and the papillary muscles. The MV constituent parts have relatively similar densities (close to 1 m^3/kg). Consequently, the MV annulus, leaflets, and chordal structure have an identical range of intensity values in the micro-CT images. This makes it impossible to use multi-threshold segmentation to label these parts in the images. Also, the valves were sutured on an annulus holder, which we needed to outline and remove from the images, (Figure 8).

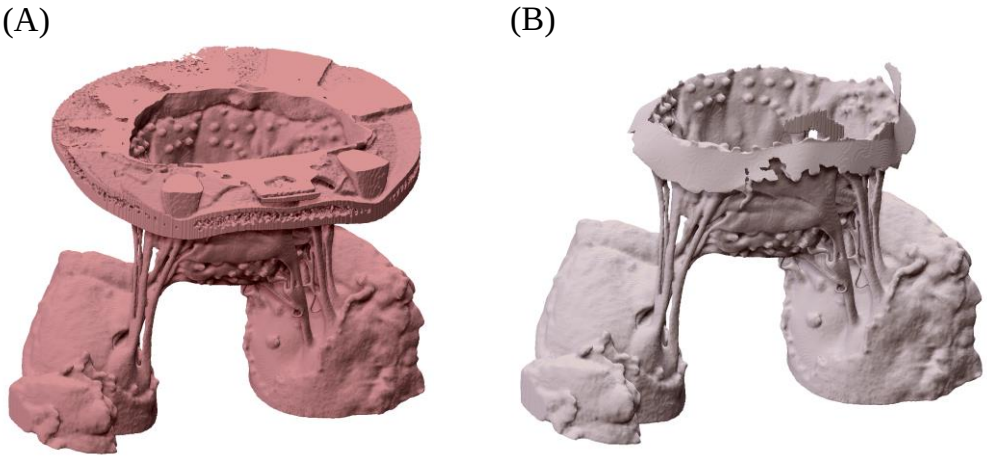

Figure 8: (A) shows the 3-D segmented image of the MV mounted on the annulus holder. The fiducial markers placed on valve annulus enabled us to outline the annulus holder and remove it by Boolean operation to acquire the MV geometry (B).

To manually label the valve constituents and detach the holder, we used the ZBrush sculpting software package (Pixologic Inc., CA, USA). The process was guided by the multi-perspective photos of the valve that we acquired from the *in vitro* setup. Ultimately, we labeled the papillary muscle heads, chordae tendineae, and leaflets in the segmented MV geometries (Figure 9).

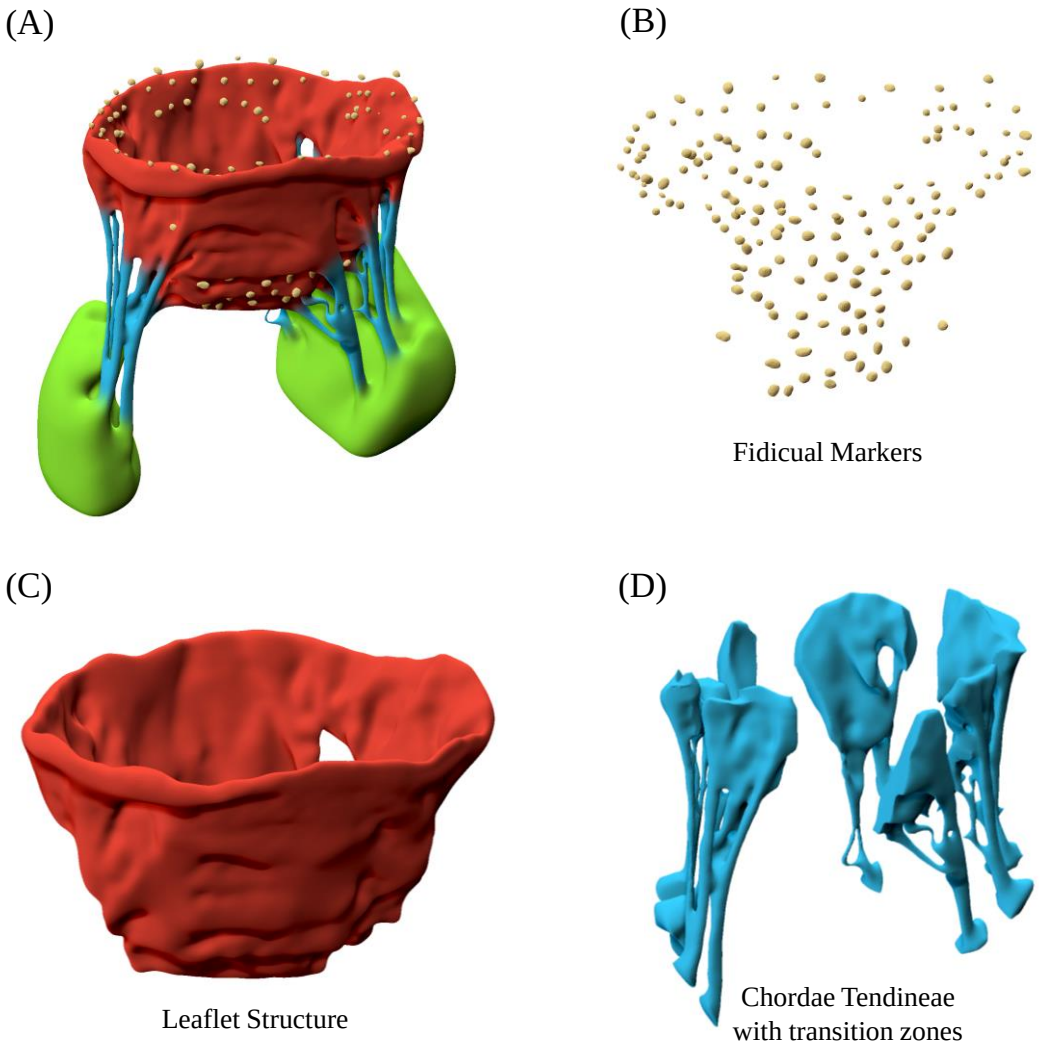

Figure 9: The MV constituent parts are labeled. (A) shows the 3-D geometry of the entire MV with leaflets (red), chordae tendineae (blue), and papillary muscles (yellow). (B) shows the fiducial markers that we placed on the valve to track the displacement of the MV in order to validate biomechanical simulations. In this study, we focused on the study of MV leaflet structure shown in (C). We are currently working on the computational anatomy of chordae tendineae shown in (D).

C. GEOMETRY MODELING

C.1. General Considerations

The object registration requires a considerable care in geometry modeling and the study of shape variations among a population. In our study, the registration of different MVs to the same coordinate system is essential for inter-subject analysis and developing a population-averaged model. We used a generalized form of superquadric shape primitives to register various MV geometries. In our pipeline, we optimized a parameter set per valve that defines a superquadric surface that captures the gross geometry of the MV (Figure 10). Consequently, this optimization registered the MV geometries in our population to a superquadric parametric space that provides a correspondence among valves. Based on this novel use of superquadrics, we co-registered our MV geometries and established an objective framework to analyze them.

Before we describe our pipeline, we note that the multi-resolution framework for geometry processing is closely related to the use of wavelets for mesh analysis (Lounsbery, DeRose, & Warren, 1997). In the current study, we have pursued a similar approach and developed a processing pipeline that allows controlling the level of detail in the final geometry reconstruction (Eck et al., 1995). However, we replaced the "base mesh" with a parametric shape primitive (superquadrics) and the "wavelet coefficients" with discrete harmonic (Fourier) basis functions. This novel approach enabled us to parameterize the complex MV geometry, quantify the fine-scale geometric features, and also build a correspondence between various MVs. We discuss our modeling pipeline in extensive detail in the rest of this section.

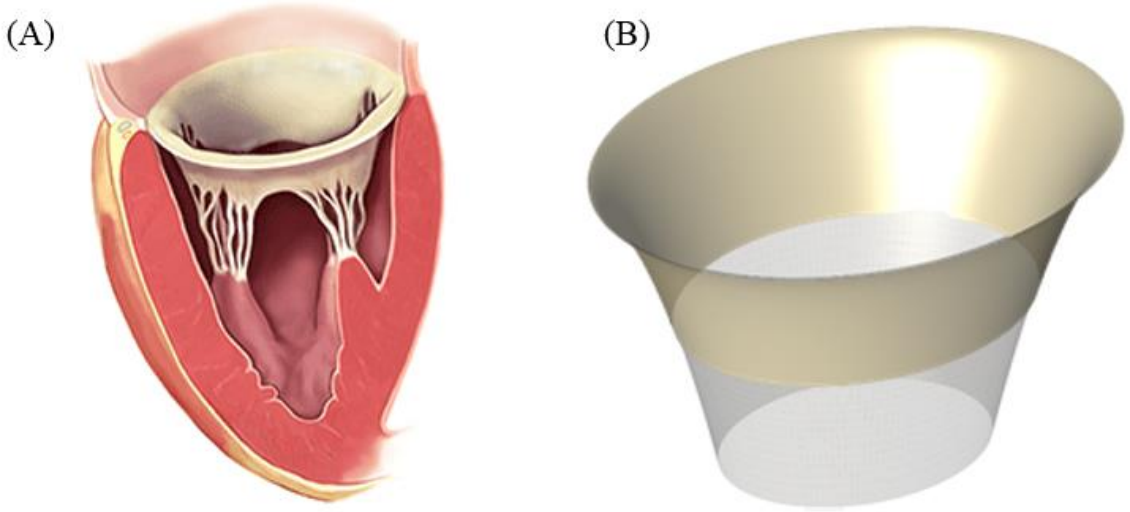

Figure 10: (A) demonstrates a schematic representation of the MV apparatus (Adapted from (A. Carpentier, Adams, & Filsoufi, 2011). (B) Indicates that the general shape of the MV leaflets can be captured by a parametric surface reconstructed with a relatively small number of parameters.

C.2. Multi-resolution Framework

We developed a pipeline to analyze the MV shape and quantify physical attributes such as geometric features in a multi-resolution framework. In our analysis, we decompose the image-based geometry of the MV into two models: (1) a basic parametric model that approximates the general MV shape, and (2) high-resolution discrete maps that capture the details of the MV surface. For the first model, we used superquadrics, which are powerful shape primitives, to describe the MV geometry with a few physically meaningful parameters (Jaklic, Leonardis, & Solina, 2013). For the second part, we relied on spectral approaches, which enabled us to reconstruct the MV atrial and ventricular surface details and control the spatial resolution in the final model reconstruction. In this work we have only studied the MV surface details, which basically form a scalar attribute. This framework can be directly applied to incorporate higher-order attributes like tensor representations of the internal fiber architecture into MV computational models.

C.3. Parametric Approximation (Superquadric Model)

C.3.a. Overview

In this section, we briefly survey the properties of superquadric shapes and our approach to modeling the MV geometry with superquadric surfaces. Superquadrics are a generalization of quadric surfaces such as spheres, ellipses, and hyperbolas introduced by Barr ((Barr, 1981)). These surfaces have been used extensively to model man-made geometries (Terzopoulos & Metaxas, 1990). Some studies have shown that superquadrics can also be successfully used to model anatomical geometries, such as the left ventricle of the heart (Bardinet, Cohen, & Ayache, 1996). We refer the reader to a review of the properties in Appendix D.

We computed a superquadric model for each studied MV by solving a non-linear least square optimization problem. There are several cost functions suggested in the literature for fitting superquadric surfaces (Solina & Bajcsy, 1990). However, they are suited for modeling shapes that are topologically equivalent to a sphere while the MV geometry has a genus-1 topology (Figure 11). Thus, we designed a novel objective function to capture the complex geometry of the MV using superquadric models. Our objective function is based on the generalized superquadric formulation that allows shape registration along with searching for the best shape description (Jaklic et al., 2013). We modified the general superquadric formulation and fixed the z-axis since our geometries were registered to a unique vertical axis in the imaging setup:

$$F(x,y,z)=\left[\left(\frac{\cos\theta(x-x_0)-\sin\theta(y-y_0)}{a_1}\right)^{2/\varepsilon_2}+\left(\frac{\sin\theta(x-x_0)+\cos\theta(y-y_0)}{a_2}\right)^{2/\varepsilon_2}\right]^{\varepsilon_2/\varepsilon_1}+\left(\frac{z-z_0}{a_3}\right)^{2/\varepsilon_1} \quad (1)$$

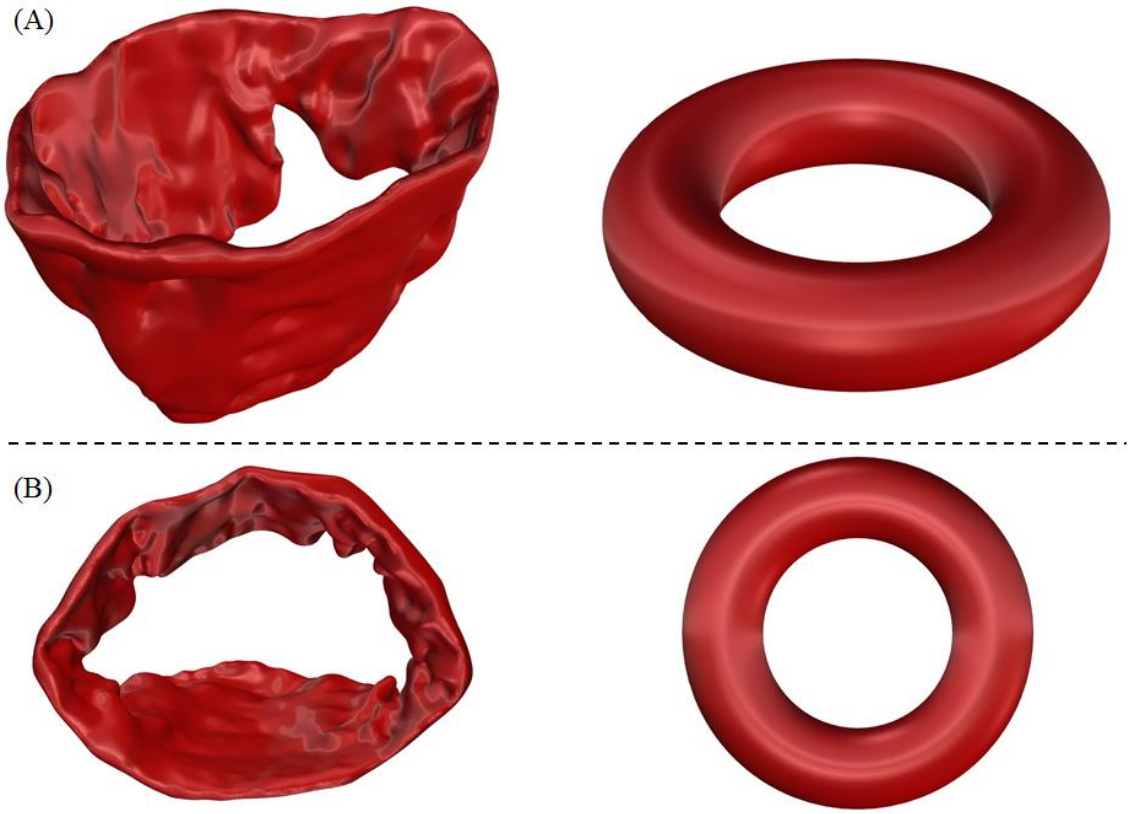

Figure 11: The MV leaflet structure is topologically analogous to a torus. This means that the MV leaflet structure is considered to be from the family of geometrical objects that have one hole (genus-1). Panel (A) shows the 3-D view of the MV leaflets and a torus. Panel (B) shows the same shapes from top view.

In equation (1), the parameters a_1, a_2, and a_3 adjust the size of the superquadric shape along x, y, and z directions, respectively. The parameters ε_1 and ε_2 are often called squareness parameters and regulate the curvature of the superquadric surface in xy-plane and long z-axis. As it might be interpreted from the form of the equation, the three parameters x_0, y_0, and z_0 are the coordinates of the coordinate system origin. Finally, the parameter θ adjusts the pose of the superquadric shape about the z-axis. The implicit equation that defines the superquadric, equation (1), is directly proportional to the signed radial distance with respect to the superquadric surface; it is negative for the points inside

the superquadric shape and positive for the points outside of it. Therefore, it is often called the superquadric inside-outside function and is used to compute superquadric models since it provides a measure of how close a superquadric model is to an input geometry.

C.3.b. Objective Function

We used three main components to devise our objective function suitable for capturing the MV geometry using a superquadric model:

$$C_1 = \left(F^{\varepsilon_1} - 1\right) \tag{2}$$

$$C_2 = \sqrt{a_1 a_2} \tag{3}$$

$$C_3 = a_3^{1/\varepsilon_1} \tag{4}$$

$$R = C_2 \times C_3 \times C_1 = \sqrt{a_1 a_2}\, a_3^{1/\varepsilon_1} \sum_i \left(F_i^{\varepsilon_1} - 1\right) \qquad i : \textit{index of input points} \tag{5}$$

To design an objective function for computing superquadric shapes, we used the inside-outside function, equation (1), as the core element of the objective function to assure the proximity of the input geometry and the computed superquadrics. The value of inside-outside function is directly proportional to radial distance from the superquadric surface, (Figure 12).

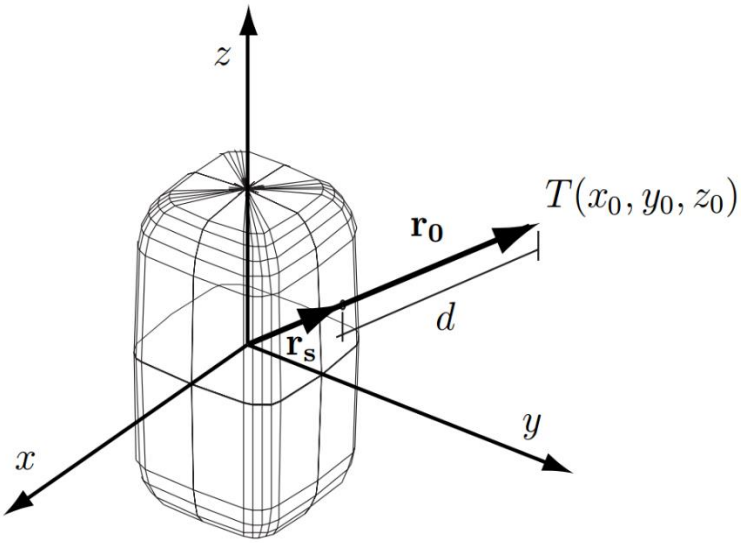

Figure 12: the superquadric inside-outside function evaluated at an arbitrary point of the 3-D space is directly proportional to the r_0 / r_s ratio for that point. Consequently, the deviation of this function from 1 can be used in the design of an objective function to compute superquadric models, (Schematic adapted from (Jaklic et al., 2013)).

Next, we penalized the proximity factor, equation (2), by multiplication with a size factor, equation (3), and a curvature factor, equation (4), to develop our objective function, equation (5). The curvature penalty component controls the convexity of the superquadrics surface (Figure 13). This specific way for penalizing the inside-outside function allows modeling hourglass geometries through least square minimization. Specifically, the curvature penalty term enables the objective function to search for structures of revolution around z-axis effectively.

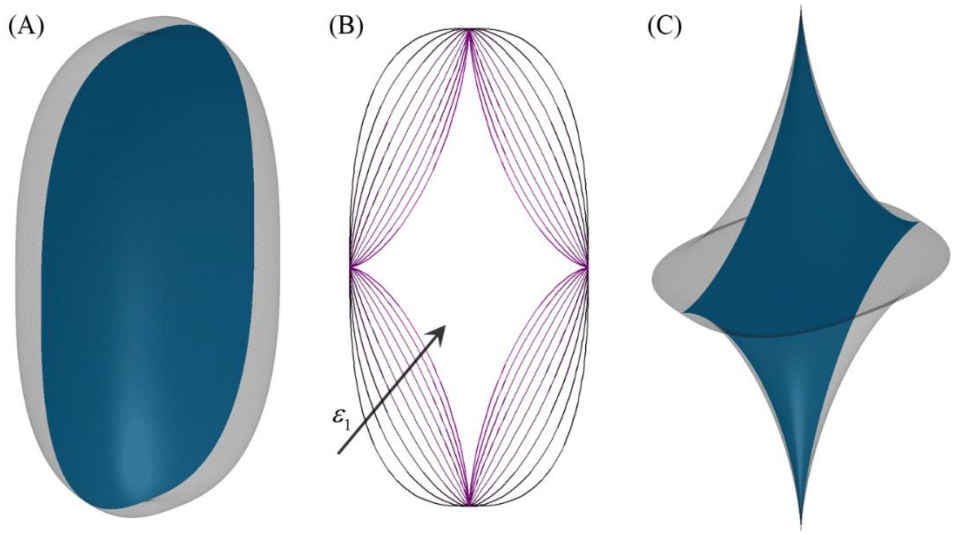

Figure 13: Curvature penalization allows capturing the MV hourglass geometry. (A) shows a representative superquadric model that would be computed without imposing the curvature criterion. (B) indicates how the curvature factor modifies the shape of a superquadric model. (C) represents a superquadric model analog to the MV leaflet geometry that is resolved by introducing curvature penalty.

C.3.c. Optimization Algorithm

We used a trust region algorithm with Levenberg-Marquardt-Fletcher (LMF) method as its core to optimize our objective function and compute superquadric models. Our objective function, equation (5), is highly non-linear and non-convex. This makes the optimization problem ill conditioned and often computationally intractable. We verified the accuracy of our solution by scanning the solution space of the optimization problem. However, the objective function has 9 parameters which makes the visualization of the convex behavior of the optimization problem impractical. Here we have included the contour plots of the objective function for changing shape parameters (Figure 14) and the annular dimensions (Figure 15). The behavior of the objective function suggests that our optimization algorithm converges to an identical family of superquadric shapes.

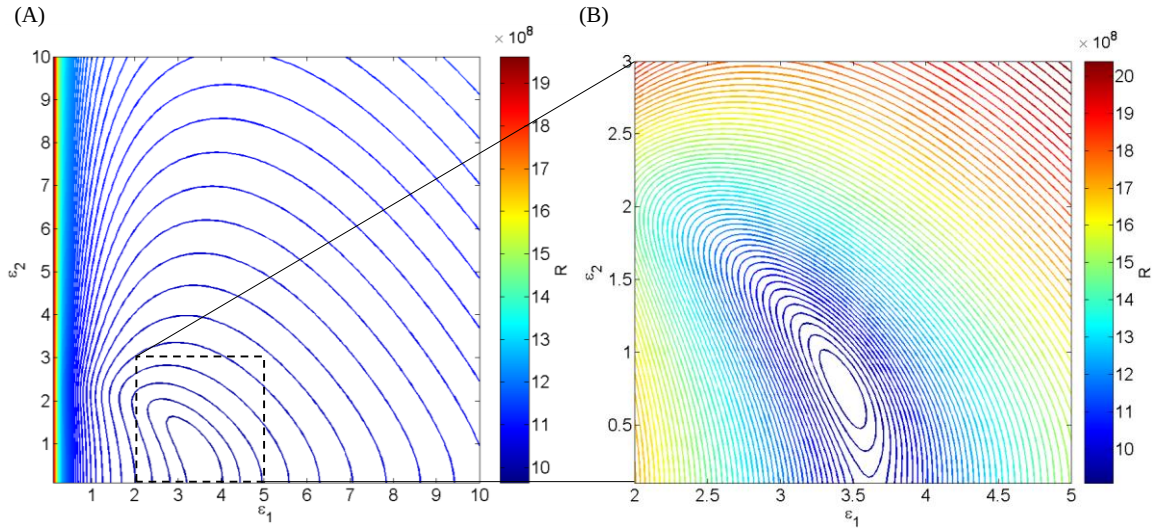

Figure 14: The behavior of objective function with respect to shape parameters is demonstrated. The high density of iso-contours in plot (A) depicts the highly non-linear behavior of the objective function. Plot (B) shows the convex solution neighborhood in the optimization problem.

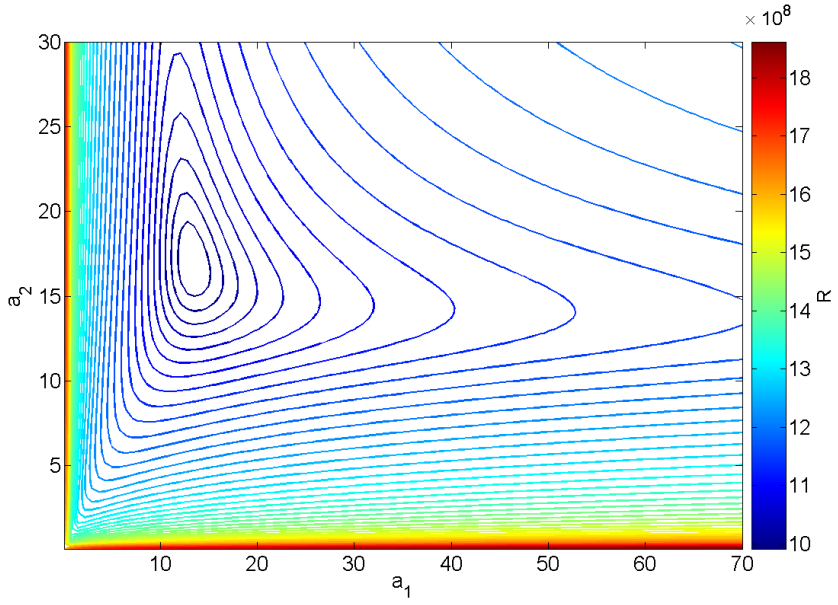

Figure 15: The objective function R is plotted versus the superquadric parameters a_1 and a_2, which denote the size of superquadric model in x and y directions respectively. This behavior suggests convexity of the objective function with respect to these parameters.

The LMF method approximates the non-linear objective function with a quadratic model, which is considered to be a valid model over a restricted region (the trust region), (Yuan, 2000). Next, the LMF method solves for the optimal point in that region through a combination of vanilla gradient decent and Newton-Gauss methods (Moré, 1978). Iteratively, the trust region is updated and a new approximation of the objective function is used until an acceptable optimal point is obtained. In our case, the objective function resembles quadratic functions in behavior since it is based on the superquadrics inside-outside function. Consequently, the quadratic approximation of the objective function and the use of LMF method led to a consistent numerical scheme.

C.3.d. Optimization Constraints

We defined semi-empirical bounds to constrain the parameter set in our optimization problem. To make the shape physically valid, the size parameters a_1, a_2, and a_3 were set to be positive values. We chose the $[0, \pi]$ interval, instead of $[0, 2\pi]$, as the search space for the angle parameter θ due to the rotational symmetry in the superquadrics shape. For the origin location x_0, y_0, and z_0, we imposed the search space to be along the z-axis by enforcing x_0 and y_0 to be zero. This imposed our *a priori* knowledge that the valves are registered to a global z-axis in the imaging setup. For the shape parameters, we set them to be positive to avoid degenerate shapes. Setting the objective function and the inequality constraints, we solved the optimization problem in MATLAB (Mathworks, MA, USA) with the convergence criterion summarized in Table (Table 3).

Table 3: Optimization setting in MATLAB for the trust-region-reflective algorithm

Function Loop Max Iterations	Outer Loop Max Iterations	Function Change Tolerance	Step-size Change Tolerance
1000	1000	1×10^{-15}	1×10^{-13}

C.4. Geometry Partitioning

We subdivided each MV mesh into two separate parts denoting the atrial and ventricular sides of the valve geometry. The mesh partitioning was required to outline two distinct meshes so the geometric features of each side could be modeled separately. However, this task becomes non-trivial as the standard curvature-based partitioning algorithms (Mangan & Whitaker, 1999) encounter issues for the study of MV geometry (Figure 16).

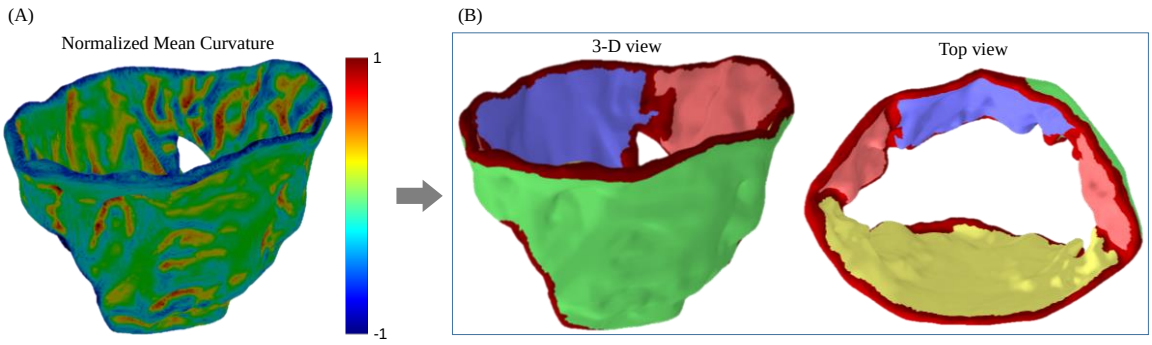

Figure 16: Curvature-based mesh partitioning for MV geometry cannot classify the mesh triangles into atrial and ventricular sides effectively. (A) shows the normalized mean curvature evaluated at the MV mesh vertices. In (B) we have shown the result of curvature-based mesh partitioning from two views. Although we expect to categorize the mesh triangles in atrial and ventricular groups, the curvature-based methods results in multiple clusters. This happens due to the fact that the MV surface has many bumps and creases that cause issues for defining decision boundaries to delineate the atrial and ventricular sides.

We used the superquadric model of the geometry as the basis to partition the mesh and define the atrial and ventricular side meshes. The superquadric model approximates the size, ellipticity of the MV annulus, and the curvature of the leaflets through the factors that we imposed on the objective function. This suggests a correspondence between the MV mesh representation and its superquadric model. Through the fitting process, we ensured that the computed superquadric and the input geometry are aligned. Consequently, we approximated the corresponding location for the MV mesh on the superquadric surface by orthogonally projecting the mesh on the superquadric surface. This projection was implemented as an iterative bisection algorithm (Figure 17). We then classified the mesh triangles based on the relative orientation of their surface normals and their corresponding outward normals on the superquadric model. In general, the angle between the two normals is acute for ventricular triangles and obtuse for atrial triangles. This then enabled us to classify the triangles in input into two groups denoting the atrial and ventricular sides of the MV.

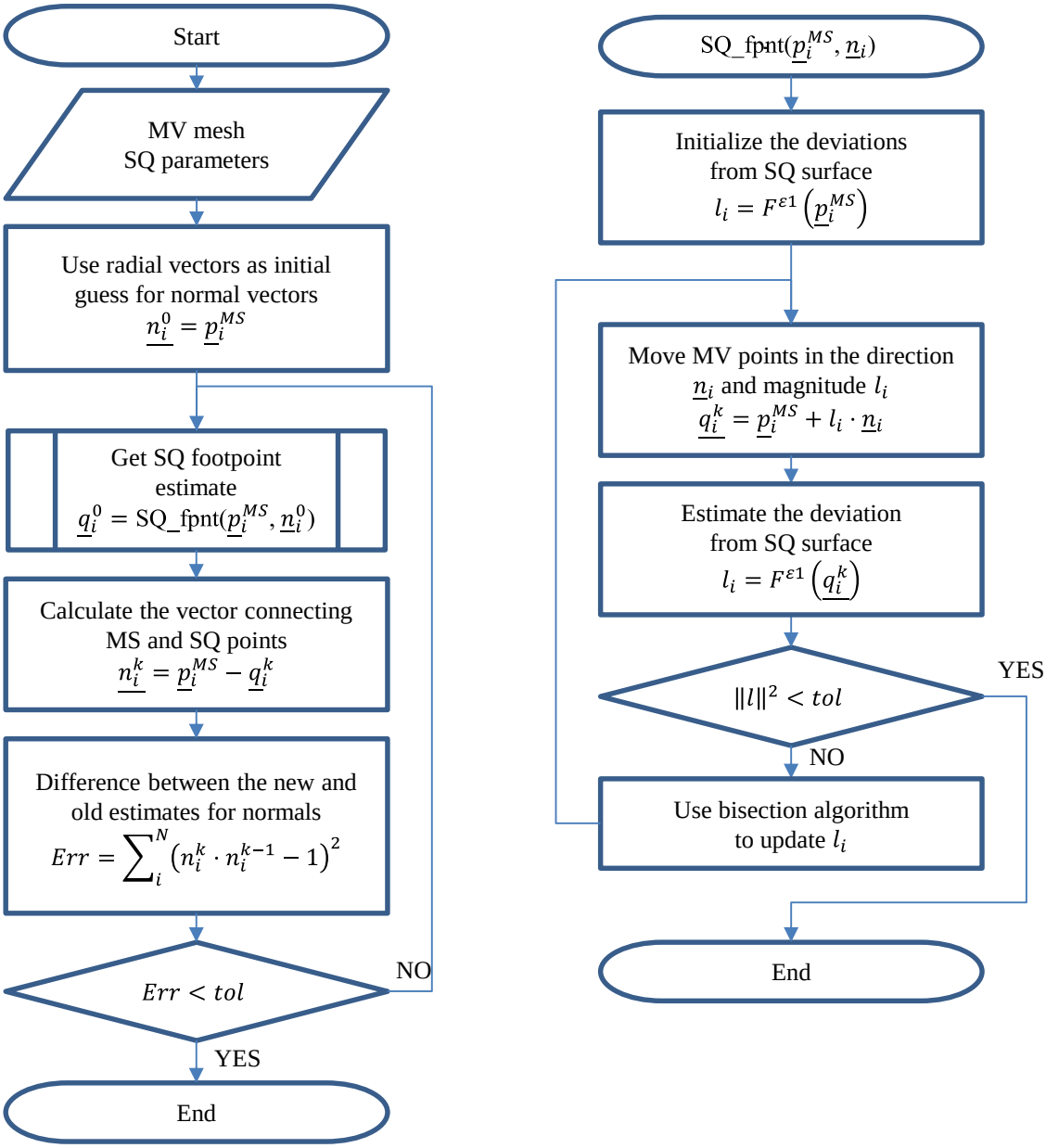

Figure 17: Iterative bisection algorithm to project a point cloud on the superquadric surface. Since we designed the projection algorithm using the superquadrics inside-outside function, the projection works well in spite of the non-convex superquadric surface.

To review, we have discussed the computation of the superquadric model and decomposing the input geometry into the atrial and ventricular parts. The set of vertices

that are shared between these two partitions denote the annulus and the free edge, which geometrically define the boundaries of the MV medial model. In the following section, we discuss the details of our novel framework for modeling the geometric details that superquadric models cannot capture. Although we have focused on the surface details here, we want to underscore that any other attribute can be modeled and assimilated with the MV geometric models using this framework.

C.5. Modeling Geometric Details (Harmonic Reconstruction)

C.5.a. Geometry Decomposition

We used an additive decomposition of the original geometry to construct a model that recovers the geometric details of the MV. In our framework, we used superquadric shape primitives to approximate the geometry of the MV and register it with a global coordinate system. However, the superquadrics provide only a basic surface representation for the 3-D geometry of the MV (Figure 18).

Although this might be sufficient for the purpose of most biomechanical simulations, our focus was to develop a pipeline to quantify the MV physical attributes and integrate them with the parametric representation (Figure 19). The geometric details of the MV surface are the simplest kind of attributes, which are required to build a medial representation of the MV geometry. Thus, we considered the superquadric model to be only a first-order approximation of the MV geometry (Figure 20).

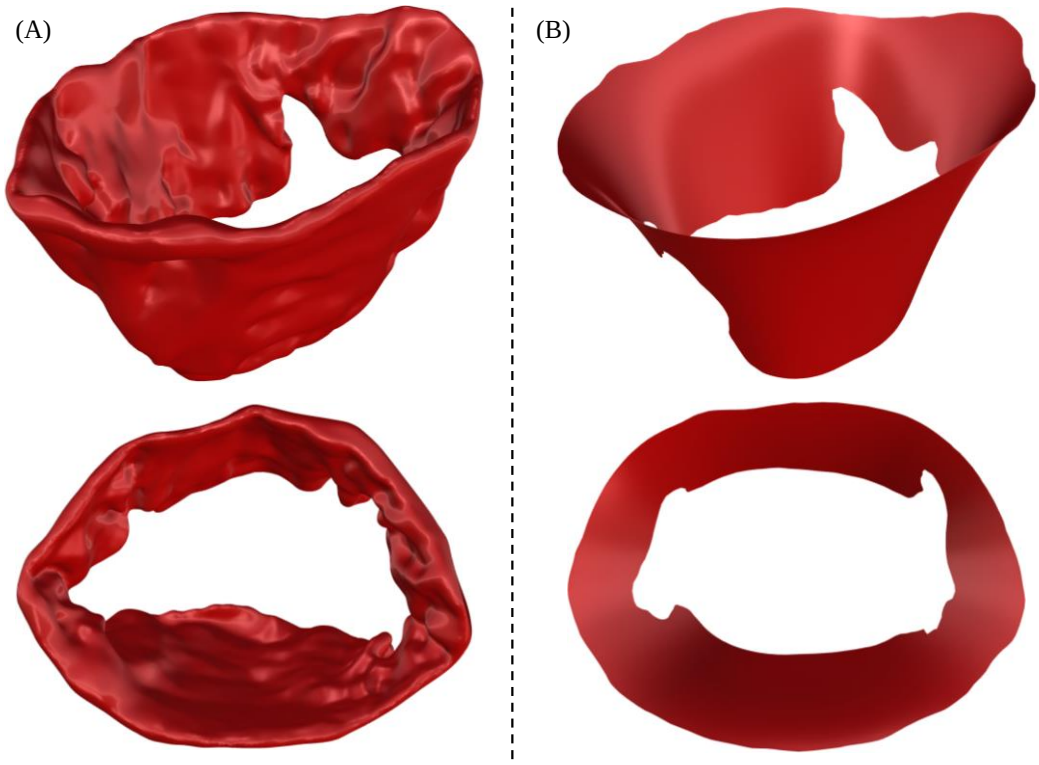

Figure 18: the MV leaflet geometry, Panel (A), can be approximated with a superquadric surface fit shown in Panel (B). The superquadric fit provides an estimation of the MV size and shape. However, by definition, it cannot capture the regional thickness and features of the MV leaflet surface.

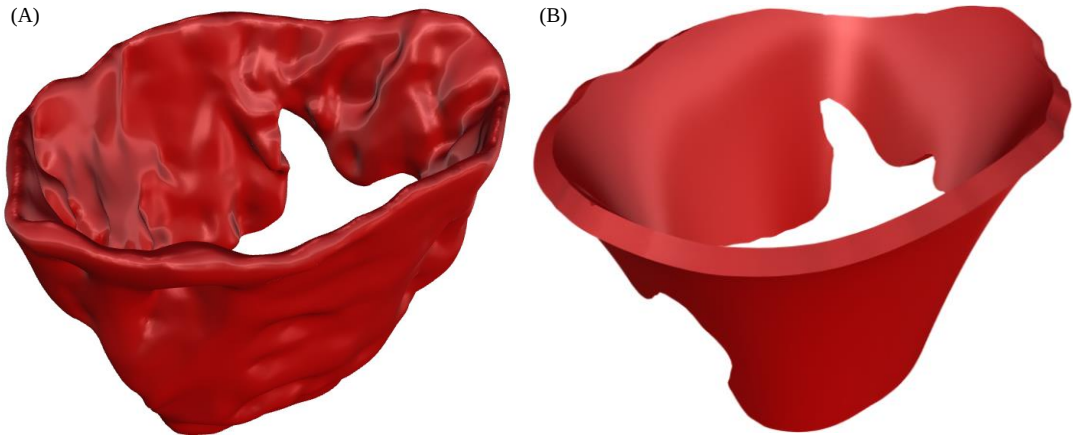

Figure 19: In our framework, we considered the superquadric model to be a first-order approximation of the 3-D MV geometry. For the purpose of most biomechanical simulations the superquadric surface fit can be used, shown in (B), to build a 3-D basic model of the input geometry, shown in (A).

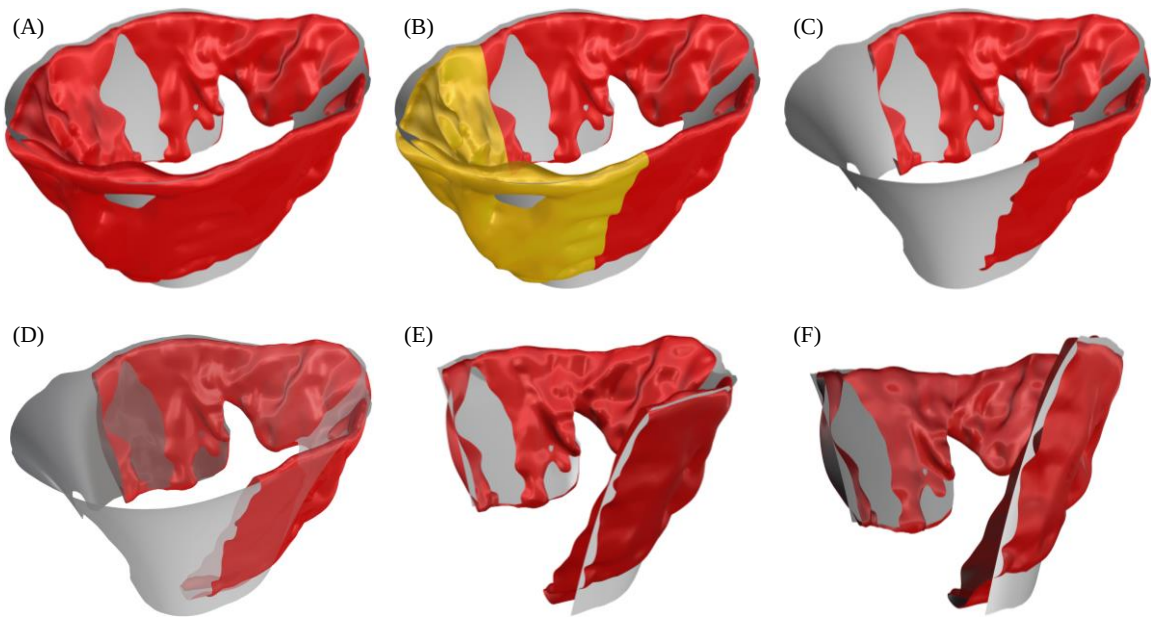

Figure 20: the superquadric approximation of the MV leaflets structure provides a basic parametric model for the valve geometry. (A) shows a representative MV geometry and a superquadric model that approximates the MV shape; (B) to (E) illustrate generating a cross sectional view of the MV leaflet structure and its superquadric model. (F) indicates the fact that a superquadric model only provides a basic approximation of the MV geometry. It also illustrates the degree to which the 3-D geometry of the MV might be different from its superquadric model.

To reconstruct the MV geometry with high fidelity, the superquadric approximation needs to be enriched by incorporating geometric details. We calculated the point-wise distance between the input geometry in our pipeline and the superquadric model to capture the fine features of the MV surface. This is similar to the bump mapping technique, which is a standard tool in computer graphics to simulate geometries with sophisticated surface details (Blinn, 1978). In our framework, we calculated the signed L_2 distance between the superquadric model and the input geometry to define the deviation fields that denote the

MV surface details (Figure 21). This distance field model the fine geometric features of the valve surface that the superquadric model cannot capture.

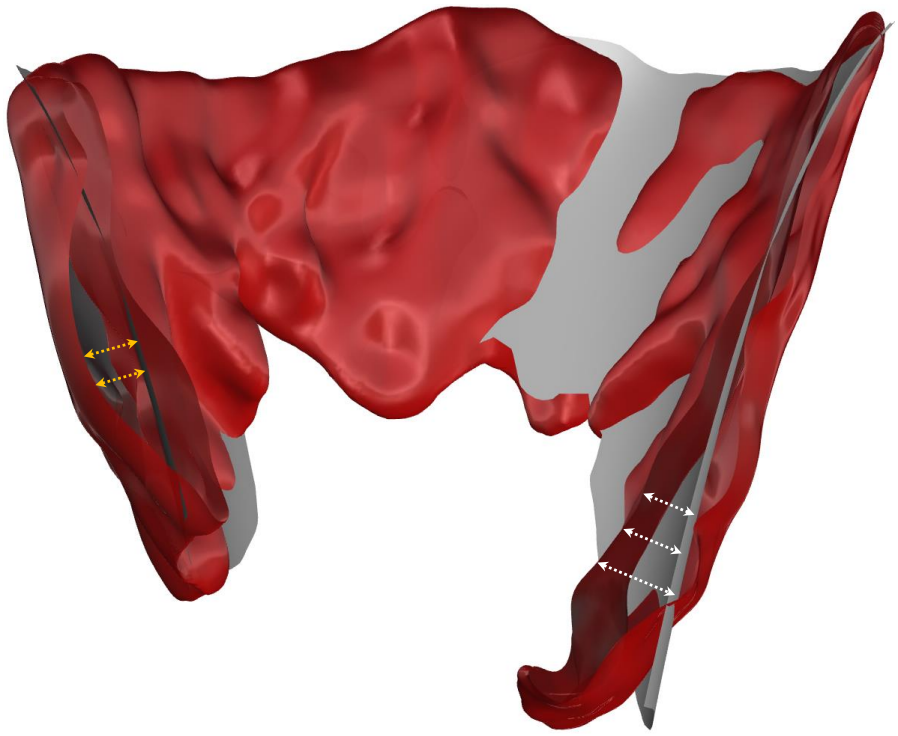

Figure 21: to capture the MV geometric details, we evaluated the deviation of MV atrial and ventricular sides from the computed superquadric model of the MV leaflets. White and yellow arrows refer to the normal distance of the MV atrial and ventricular sides from the superquadric model respectively. To reconstruct the MV geometry with high accuracy, we modeled these normal distances as scalar fields defined on the parametric domain of the superquadric surface.

There are two deviation fields per valve denoting the geometric details, which correspond to the atrial and ventricular sides of the MV leaflets. To define each field, we first projected the corresponding mesh orthogonally onto the superquadric model using our iterative bisection method (Figure 17). This enabled us to build a correspondence between the input geometry and the parametric superquadric model, (Figure 22).

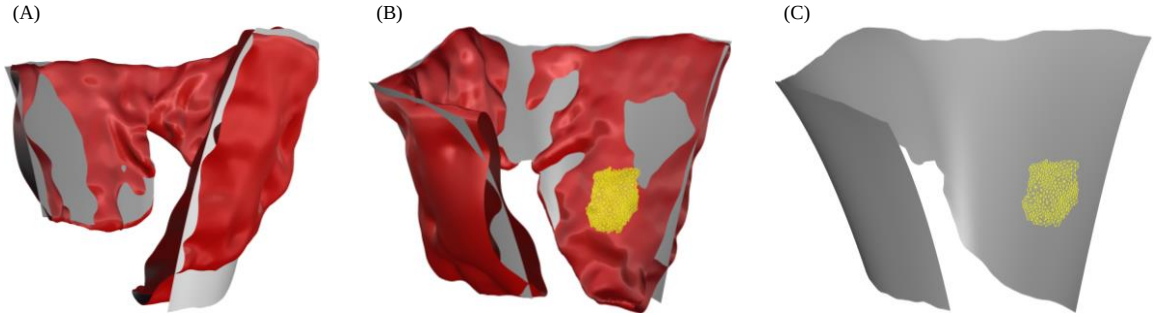

Figure 22: the procedure to define the domain of the MV geometric details is illustrated. The MV surface features can be quantified as deviation fields that consist of the L_2 distance between the input geometry and the superquadric model. Plot (A) illustrates the location of our cross sectional view. Plots (B) shows a highlighted region on the input mesh. The same projection of this highlighted region on the superquadric model is shown in (C). The point-wise distance between the input mesh and the projected one denotes the geometric details of the MV surface.

Then, we parameterized the projected mesh according to the parametric representation of the superquadrics model:

$$\begin{cases} \eta = \left[\sin^{-1}\left(\left| \frac{z}{a_3} \right| \right) \right]^{1/\varepsilon_1} \operatorname{sgn}\left(\frac{z}{a_3} \right) \\ \omega = \tan^{-1}\left(\frac{\left| \frac{y}{a_2} \right|^{1/\varepsilon_2} \operatorname{sgn}\left(\frac{y}{a_2} \right)}{\left| \frac{x}{a_1} \right|^{1/\varepsilon_2} \operatorname{sgn}\left(\frac{x}{a_1} \right)} \right) \end{cases} \tag{6}$$

In equation (6), the input Cartesian coordinates of the MV mesh after projection on the superquadric surface *(x, y, z)*, are transformed to the parametric domain of the superquadrics surface *(η, ω)*. This parametrization is in fact a conformal map from the 3-

D Cartesian space, onto the 2-D periodic domain of the superquadric surface. An intuitive way to visualize this parametrization is to consider it as unfolding of the MV mesh projected on the superquadrics, on a 2D plane (Figure 23).

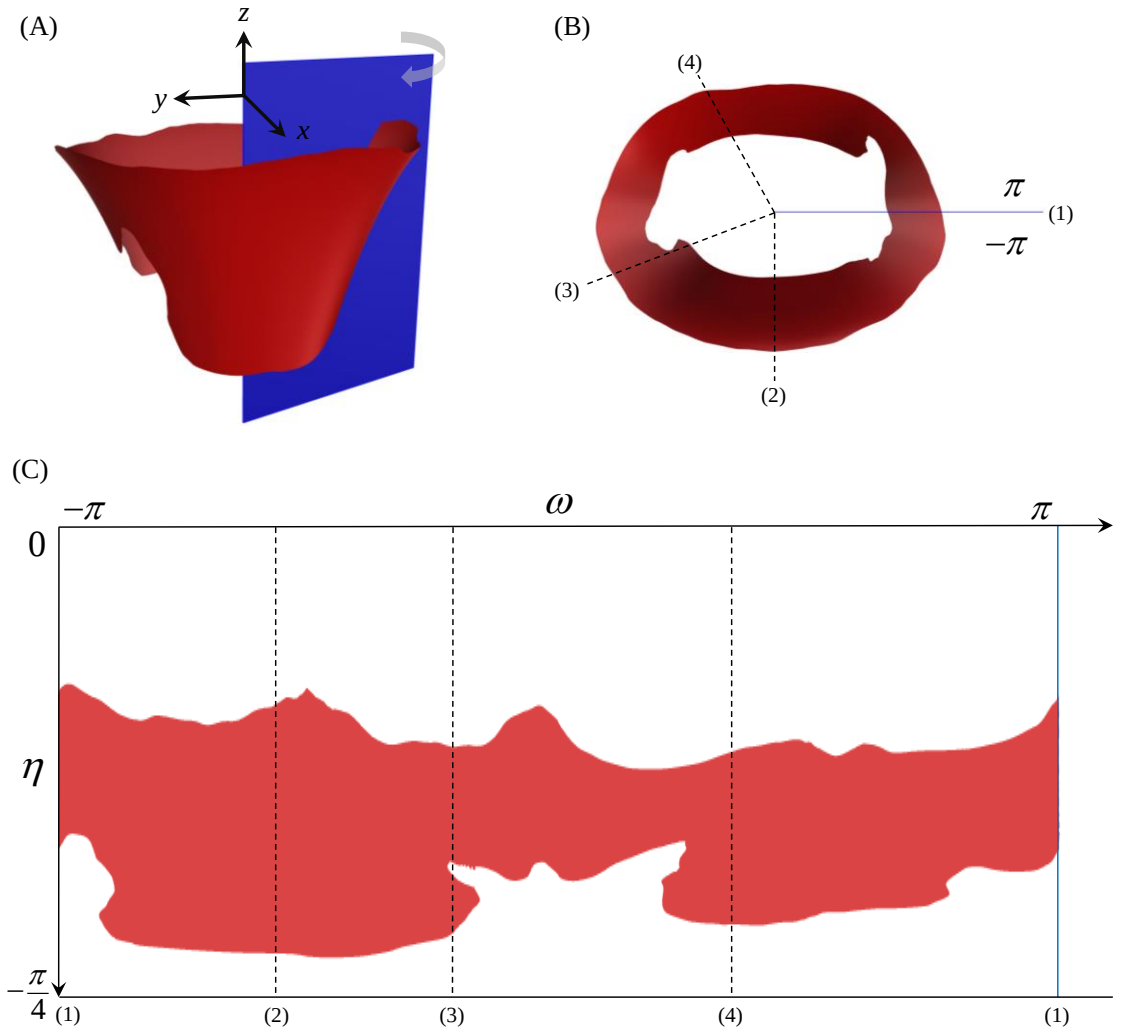

Figure 23: (A-B) Representative MV mesh projected on the superquadric model, with periodic boundary highlighted in blue. (C) Plot of the MV mesh projected on its parametric space. This mapping 3-D Cartesian space to the 2-D parametric domain of the superquadrics allowed us to reconstruct the geometric details of the MV surface in a way that can be integrated with the superquadric model. The MV geometry occupies a narrow region in the parametric domain so it has been shown on a section of the space *(-π/4<η<0)*.

Ultimately, the projection and subsequent parametrization enabled us to model the geometric details as a scalar function defined on the 2-D surface of the valve's superquadric model. The conformal property of the superquadric parameterization allows performing a harmonic spectral analysis to reconstruct the geometric details of the MV surface in the superquadric domain. This conformal property is required to pull back the reconstruction on the 2-D parametric domain onto the 3-D surface of the superquadric model. More importantly, this property of the superquadrics allows us to model higher-order attributes like vector fields using the same framework. Namely, the fiber architecture information acquired by light scattering techniques (Sacks, Smith, & Hiester, 1997) can be assimilated with the geometric representation of the MV using our modeling framework. In the following section, we discuss our framework to reconstruct the MV geometric details defined as a scalar attribute that denotes deviation of actual MV surface from the superquadric model.

C.5.b. Spectral Analysis

C.5.b.i. Overview

We used spectral analysis to describe the deviation of the superquadric model from the actual MV geometry. Specifically, the residual fields between the superquadric model and the two MV surfaces were reconstructed as a sum of Fourier basis functions defined by

$$f(\eta,\omega) = \Sigma\Sigma F(n,m)e^{-2\pi i(n\eta+m\omega)} \tag{7}$$

$$e^{-2\pi i(n\eta+m\omega)} = \cos\left(-2\pi\left(n\eta+m\omega\right)\right) + i\sin\left(-2\pi\left(n\eta+m\omega\right)\right) \tag{8}$$

In equation (6), f represents the scalar function modeling the MV geometric details and F is its Fourier transform. The exponential term, equation (7), is in fact the Euler representation of Fourier basis function. In this formulation, the MV attributes are modeled in the frequency domain and then reconstructed back in the spatial domain and imposed on the superquadric model. This approach has three main advantages as discussed below.

First, we wanted to add the geometric details to the parametric superquadric model of the valve and reconstruct the surface geometry with high fidelity. Thus, we needed to register the deviation fields to the same parametric domain as the superquadric model. The deviation values prior to spectral analysis are merely a discrete sampling of the residual field, since deviation values are only defined at the MV mesh vertices (Figure 24). Through equation (6), however, we arrive at a continuously defined representation of the residual field, which allows us to approximate the actual MV surface geometry at any coordinate pair (η, ω).

Second, the reconstruction enables us to define the deviation fields independent of their mesh domain and gridding. This facilitates averaging the atrial and ventricular deviation fields to construct a medial representation of the valve geometry. The medial representation with local thickness is essential to simulate the MV using shell or solid elements. Moreover, the spectral reconstruction allows resampling the deviation fields with an adjustable resolution. Accordingly, our pipeline provides a framework to reconstruct MV computational models with any desired discretization required for sensitivity analysis.

Last and most notably, the reconstruction using Fourier basis functions allows averaging the geometric details for different valves. This lends itself directly to developing an average model for the MV geometry enriched with average physical attributes. Applying the spectral reconstruction on multiple valves facilitates proper registration between different valves, which is the key and most challenging step in averaging properties.

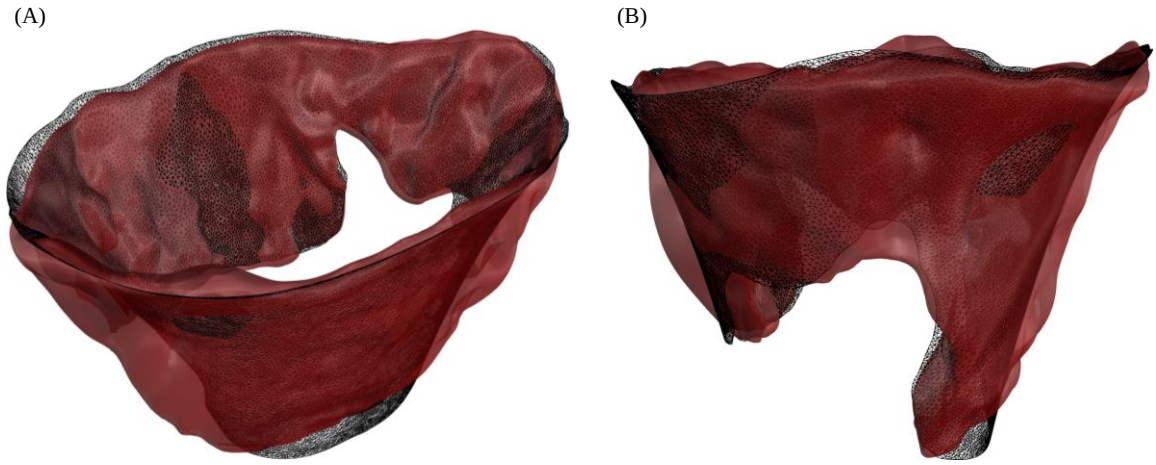

Figure 24, the irregular domain for the MV geometric details is illustrated from 2 views. To model the MV surface bumps and creases, we were required to reconstruct the pointwise distance between the input geometry and the superquadric model. However, since the input geometry is defined as a triangulated surface, the distance maps denoting the atrial and ventricular surface details are defined on domains with non-uniform structures.

While these features are very appealing, performing spectral reconstruction of the fields defined on triangulated meshes is still nontrivial for two reasons: (1) the non-uniform structure of the tessellated mesh representation, (2) the free-form shape of the domain boundaries. In the rest of this section we discuss our method to overcome these challenges and reconstruct the MV geometric details.

C.5.b.ii. Non-uniform data structure

The standard Fast Fourier Transform (FFT) algorithms are not applicable to perform spectral analysis when the data is sampled irregularly (Marvasti, 2012). Essentially, the FFT algorithms require the input data to be tabulated on a Cartesian grid. In our case, the scalar fields denoting the geometric details and other attributes are defined on unstructured meshes. Consequently, none of the standard FFT implementations could

be used. Thus, we used a Non-Uniform Fast Fourier Transform (NUFFT) to perform a spectral reconstruction of the MV surface details.

To perform spectral analysis, we used an NUFFT algorithm that first oversamples the data on a Cartesian grid using truncated Gaussian kernels and then applies a standard FFT (Greengard & Lee, 2004). This approach is a subset of NUFFT algorithms that are known as gridding algorithms. It has been shown that the effect of Gaussian kernels to interpolate the data on a regular grid can be removed using the convolution theorem. Using this approach to perform Fourier analysis does not introduce interpolation errors if the data is uniformly distributed for interpolation over a rectangular domain (one 2-D period). However, because MV attributes like geometric details are defined over irregular domains, the NUFFT algorithm fails unless the shape of the domain is accounted for. In the following section, we have discussed our approach to account for the special shape of the MV boundaries that introduce errors in the NUFFT algorithm. [We have performed a survey of the available NUFFT algorithms that can be found in APPENDIX F].

C.5.b.iii. Free form boundaries

The deviation fields denoting the MV geometric details have free-form top and bottom boundaries (Figure 23). These boundaries, corresponding to the MV annulus and free edge respectively, do not coincide with the top and bottom boundaries of the superquadric parametric domain, and thus hinder the direct applicability of NUFFT. The gridding step in the NUFFT algorithm oversamples the known function values on a periodic Cartesian grid. Because our deviation fields do not occupy the entire periodic domain (Figure 25A), interpolation for NUFFT results in zero-padding in subdomains where there are no data (Figure 25B).

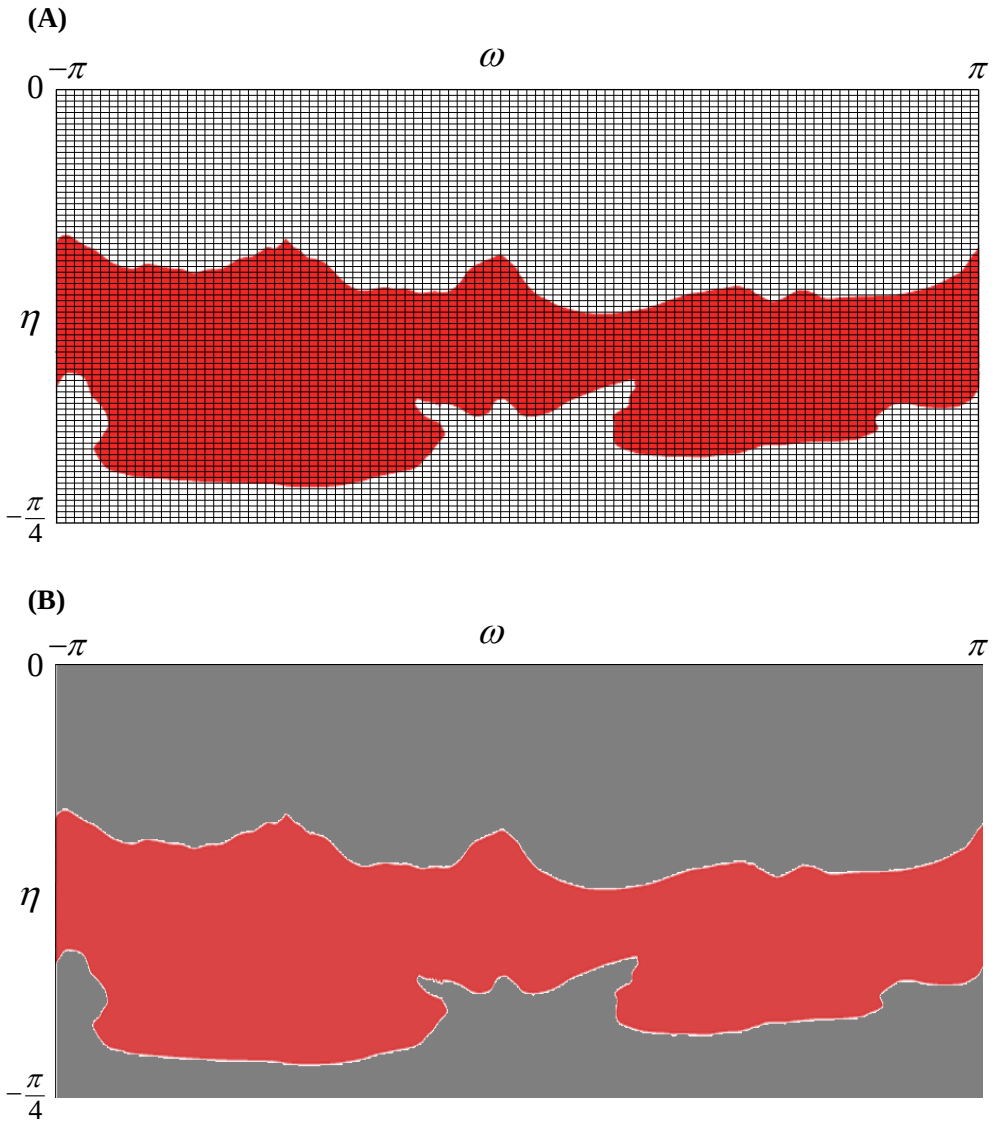

Figure 25: The Gaussian gridding approach for NUFFT interpolates the data on a super-sampled Cartesian grid shown in (A). For the MV attributes this results in zero-padding the data in subdomains of the parametric space where the MV domain is not defined, shown as grey in (B). Applying FFT for computing the Fourier transform of the interpolated function fails due to the discontinuity of data on the MV irregular boundaries, highlighted in (B).

Applying FFT on the zero-padded data results in a Fourier analysis that is drastically different from the actual frequency content of the MV geometric details. This is

due to the Gibbs phenomenon (Gottlieb & Shu, 1997) polluting the entire spectrum with noise, which is a direct artifact of zero-padding the data and causing a discontinuity at the MV boundaries. Expanding the bandwidth to attenuate the Gibbs phenomenon causes two problems: (1) the computational cost of the 2-D Fourier analysis process increases quadratically with the number of frequencies; and (2) the reconstruction of the geometric details becomes impossible as a result of the high-frequency components polluting the power spectrum.

The special shape of the MV boundaries can be modeled as a 2-D window (mask) function (Figure 26). In other words, we considered the zero-padded function in the NUFFT algorithm to be in fact the product of a periodic function and a window that is 1 inside the MV physical boundaries and zero elsewhere. The rationale behind this multiplicative decomposition is to separate the scalar fields modeling the geometric features of the MV surface from the MV boundaries.

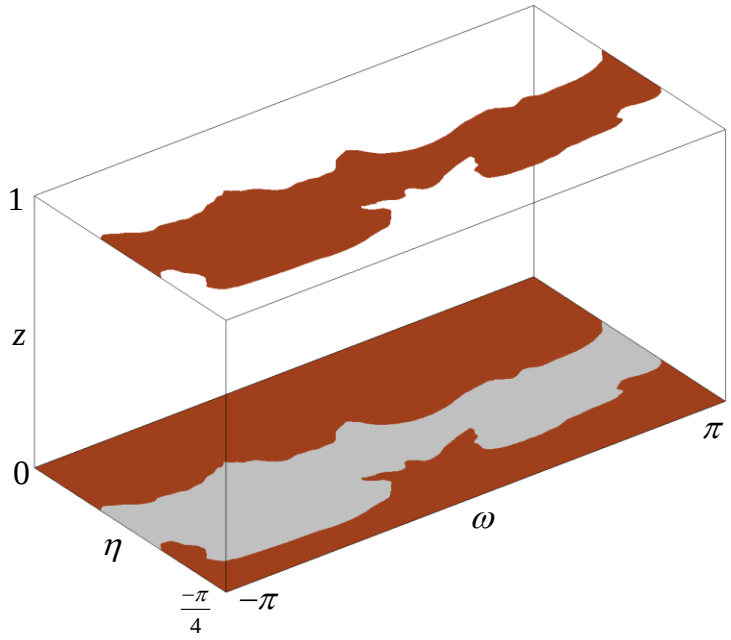

Figure 26: In Fourier reconstruction, we modeled the effect of MV boundaries as a mask shown here, multiplied by an underlying function that is defined over the entire parametric domain of superquadrics and denotes the MV geometric details. This function when sampled inside the MV parametric domain recovers the geometric details of the MV surface.

The MV leaflets as a soft biological tissue have a smooth surface, without any sharp bumps or edges. Thus, assuming the function that models the MV surface geometric features to be smooth and essentially bandlimited is certainly valid. Following this, all the high-frequency pollution in the reconstruction of geometric details can be attributed to the spectral leakage caused by the effect of windowing (Bernstein, Fain, & Riederer, 2001), which in our case models the MV boundaries. We removed this effect by limiting the number of Fourier frequencies used to reconstruct the geometric details. Consequently, we were able to remove the spurious frequency components caused by the irregular boundaries and recover a clean spectrum. In other words, the pollution resulting from the free-form boundaries was resolved by imposing a sparsity constraint on the spectral analysis. Our

implementation of sparse NUFFT to reconstruct the MV geometric details is discussed in the following section.

C.5.b.iv. Sparse Spectral Analysis

To overcome the effect of irregular boundaries, we imposed a sparsity constraint on the NUFFT algorithm to reconstruct the MV geometric details. The sparsity constraint penalizes the number of Fourier frequencies in the spectral analysis. This constraint leads to attenuating the spurious noise polluting the spectrum, caused by the irregular boundaries and thus allows recovering a clean power spectrum using NUFFT. Our method can also be viewed as an implementation of a LASSO optimization formulation to find the Fourier transform (Tibshirani, 1996). In this perspective, the objectives are: (1) maximum match with the known function values (i.e. geometric details) in the spatial domain, and (2) maximum sparsity of the power spectrum in the spectral domain. Moreover, we imposed the frequency representation for the MV geometric details to be bandlimited and solved the optimization problem for the sparse spectral reconstruction using a proximal gradient method (Parikh & Boyd, 2013).

Our iterative algorithm to perform spectral analysis is very straightforward and only requires repeating a few steps until the convergence criterion is satisfied (Figure 27). It should be noted that there are more efficient and sophisticated algorithms like the Nesterov scheme (Nesterov, 2005) to perform the Fourier transform constrained with the spectral sparsity criterion. However, we used a proximal gradient method due to its suitable convergence rate and low computational complexity of each iteration step.

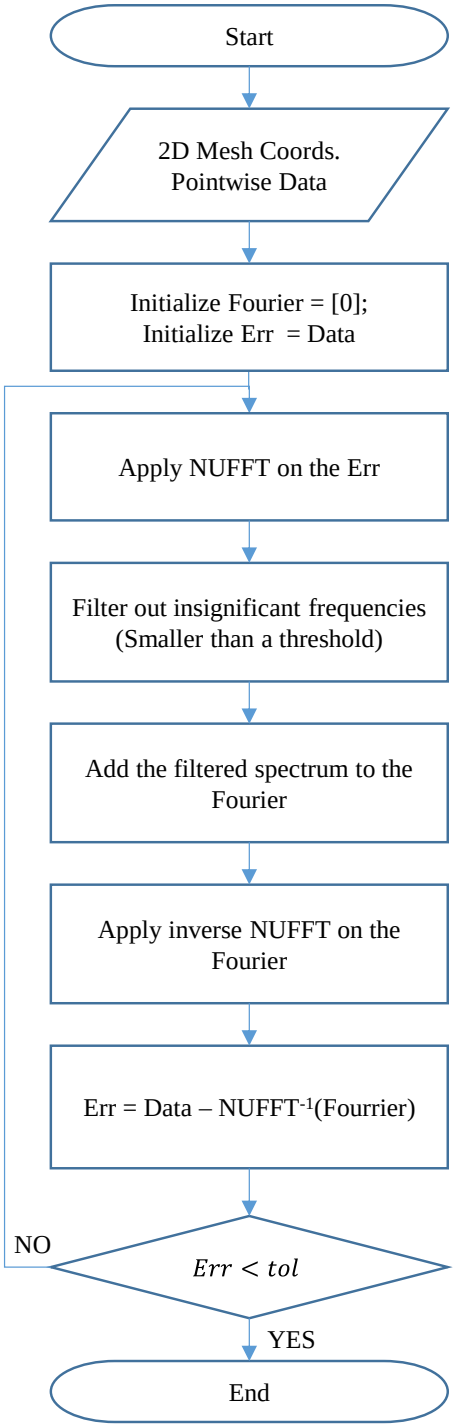

Figure 27: Our iterative approach for sparse spectral analysis is described. The algorithm requires setting a threshold for filtering the noise that is an artifact of irregular boundaries. The threshold was chosen empirically to be 1×10^{-4} for all valves.

C.6. Geometry Reconstruction

To reconstruct a detailed MV model, we superimposed the MV geometric details on the smooth superquadric approximation of the MV shape:

$$\vec{r}(\eta,\omega) = \vec{p}(\eta,\omega) + f(\eta,\omega)\cdot\vec{e}_N(\eta,\omega) \tag{8}$$

$$\vec{p}(\eta,\omega) = \begin{bmatrix} a_1\cos^{\varepsilon_1}(\eta)\cos^{\varepsilon_2}(\omega) \\ a_2\cos^{\varepsilon_1}(\eta)\sin^{\varepsilon_2}(\omega) \\ a_3\sin^{\varepsilon_1}(\eta) \end{bmatrix} \qquad \begin{matrix} -\frac{\pi}{2} < \eta < \frac{\pi}{2} \\ -\pi < \omega < \pi \end{matrix} \tag{9}$$

In equation (8), the function $\vec{r}$ denotes location of either MV atrial or ventricular side and $\vec{p}$ refers to the superquadric model of the full MV geometry. The parametric model of each side is reconstructed by deforming the superquadric surface $\vec{p}$ according to the geometric details function *f*. This superposition relation for geometry recovery follows directly from the additive decomposition of the input geometry. However, our framework reconstructs the MV geometric details on the entire parametric domain. Thus, we restricted the domain in the MV parametric reconstruction, equation (9), by projecting the annulus and free edge curves on the parametric domain and outlining the original MV boundaries.

C.7. Medial Representation

The superquadric surface can only provide a basic model of the MV geometry that is different than the medial surface of the MV geometry, (Figure 28). In our framework, we modeled the deviation of the atrial and ventricular sides of the MV geometry from the superquadric surface by spectral analysis. The spectral reconstruction instantly provides the means to build a medial representation of the MV with regional thickness which is discussed as follows. In this document, we have extended the medial surface representation of the MV in the figures for better visualization while it is well noted that the medial representation does not intersect with the original geometry.

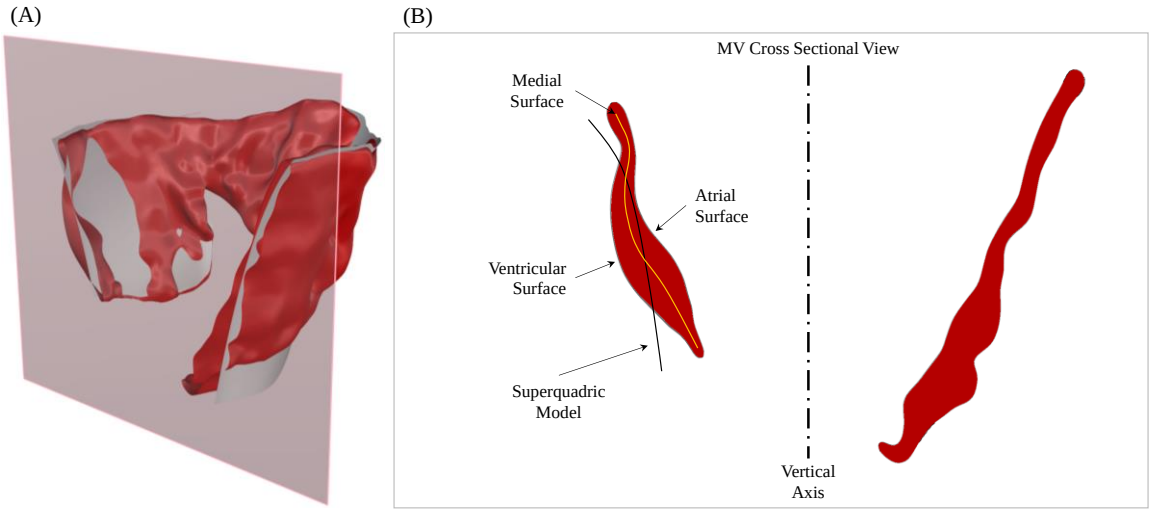

Figure 28: The discrepancy between the medial surface and the superquadric model is shown. Plot (A) represents a cross sectional view of a MV geometry modeled by a superquadric surface. This cross section is shown in normal view in plot (B). The spectral analysis in our framework allows evaluating the medial surface based on the superquadric model.

C.7.a. Medial Surface

To approximate the medial model of the MV geometry, we averaged the geometric models of the MV atrial and ventricular sides (Figure 29). This follows from the definition of the medial representation that the medial is the locus of points equidistant from the boundary contours (H. I. Choi, Choi, & Moon, 1997). The full medial representation consists of a medial surface and a thickness field that indicates the original boundaries. Acquiring the thickness field, however, requires more processing than the medial.

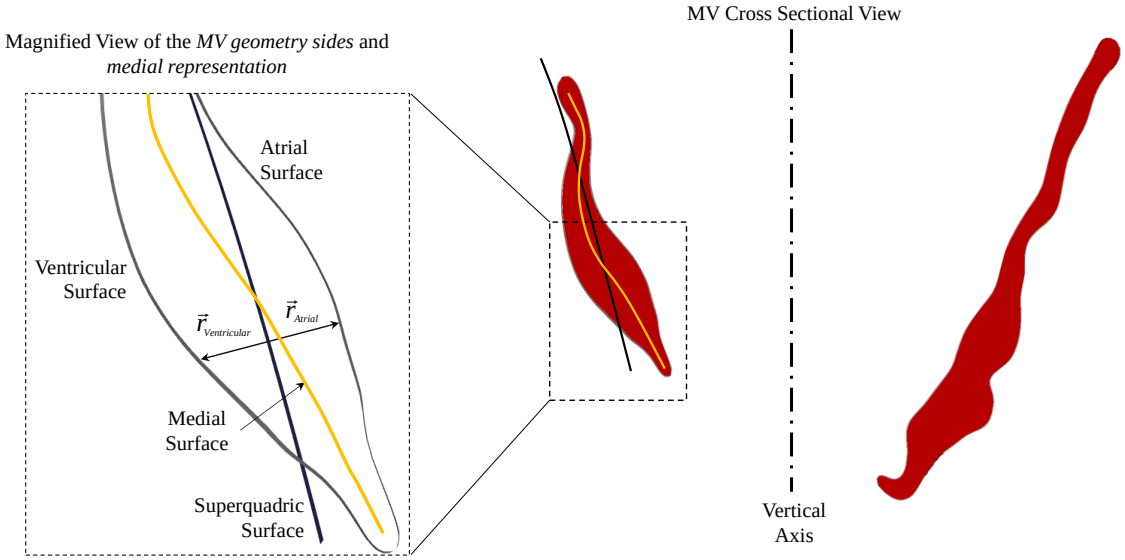

Figure 29: The medial surface location can be approximated by averaging the distance of atrial and ventricular surfaces from the superquadric model.

C.7.b Thickness Field

We computed the MV's local thickness by processing the distance of the atrial and ventricular sides of the MV from the superquadric model. By local thickness, we refer to the radius of the sphere centered on the medial that is tangent to shape boundaries (Figure 30). Based on this definition, the thickness field is proportional to the difference in the distance of the MV sides from the superquadric surface. To acquire the local thickness

values, we evaluated the projection of the difference between the atrial and ventricular deviation from the superquadric model, (Figure 31). The parametric reconstruction of the valve geometry provides an efficient mathematical basis for the evaluation of MV regional thickness by subtracting the relative distance of atrial and ventricular surfaces from the superquadric model.

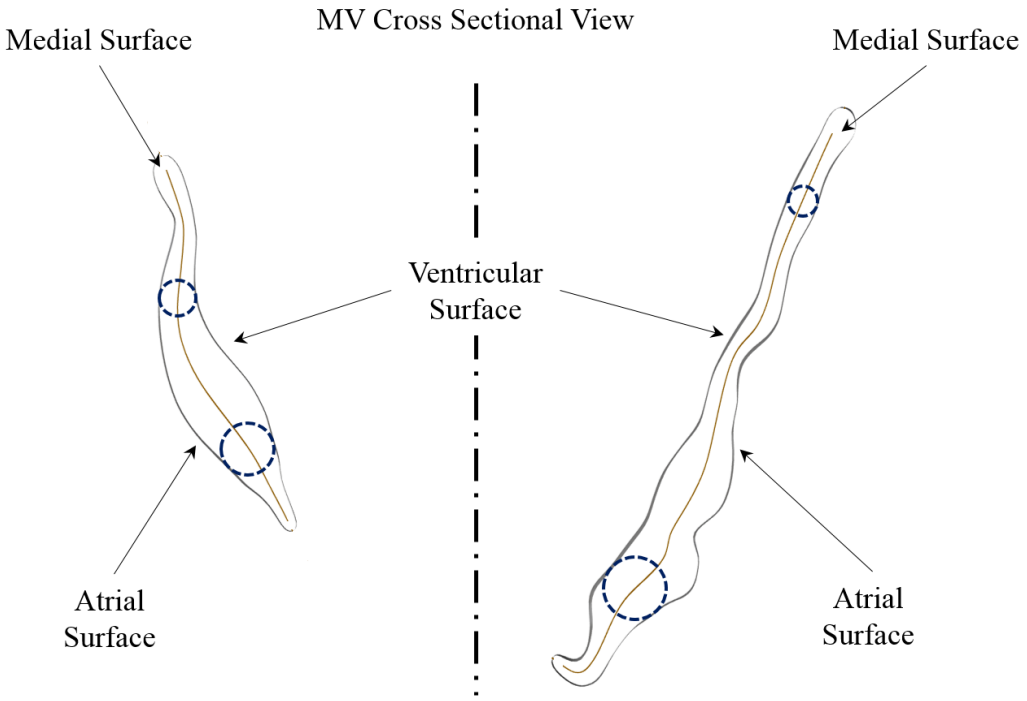

Figure 30: The MV leaflet local thickness can be defined as the radius of the spheres that are centered at the medial surface and tangent to the atrial and ventricular boundaries.

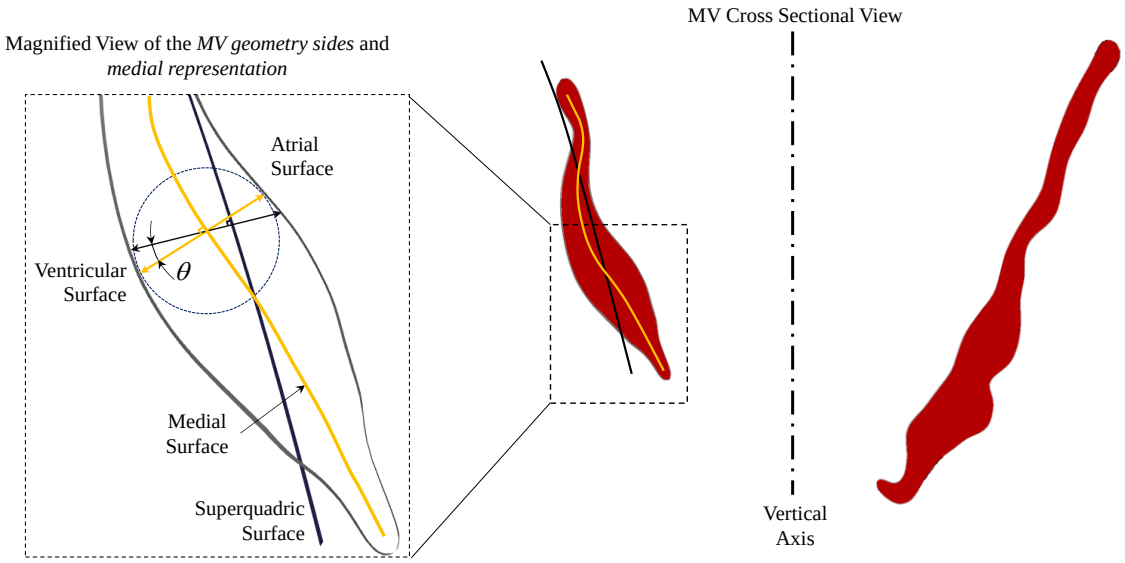

Figure 31: The normal to the superquadric surface is not necessarily in the same direction as the normal to the medial surface, shown as angle θ. The thickness field computed by using spectral reconstruction of the geometric details needs to be projected on the normal to the medial surface. This is done by multiplying the reconstructed thickness fields by $cos(\theta)$ that is evaluated pointwise on the medial surface.

Chapter 4: Results

A. Overview

This chapter is organized in three parts. First, we present the intermediate and final results of our pipeline to reconstruct the MV geometry. This provides a review of the whole pipeline, illustrated by results from modeling three MVs. Then, we review the construction medial model for a MV. Finally, we assess the accuracy of our modeling methodology and validate by comparing the input and reconstructed geometry for a MV.

We implemented our pipeline in MATLAB (Mathworks, MA, USA) and automated some computationally intensive algorithms in C++ to achieve better numerical speed. Specifically, we developed new MATALB libraries for (1) NURBS-based geometry processing, (2) mesh and graph processing, and (3) differential mesh filtering. We also used open source NUFFT libraries developed in FORTRAN by Greengard and Lee (Greengard & Lee, 2004).

B. Modeling Pipeline

In this work, we developed a novel pipeline to analyze the MV geometry in a multi-resolution framework. Our methodology is based on additive decomposition of the original geometry into two models: (1) a superquadric fit that approximates the general shape of the MV, and (2) a spectral reconstruction of the fine-scale geometric details. This framework enabled us to build computational models of the MV geometry with an adjustable density of geometric details. In this section we review the result of each major step in our geometry-modeling pipeline.

B.1. Superquadric Models

A unique superquadric surface was fitted for each studied valve, (Figure 32). The optimization procedure was carefully monitored to assure convergence to an identical neighborhood for the studied geometries. The agreement in the calculated values and convergence behavior suggests that our optimization algorithm has successfully found an identical family of superquadrics to model MV geometries.

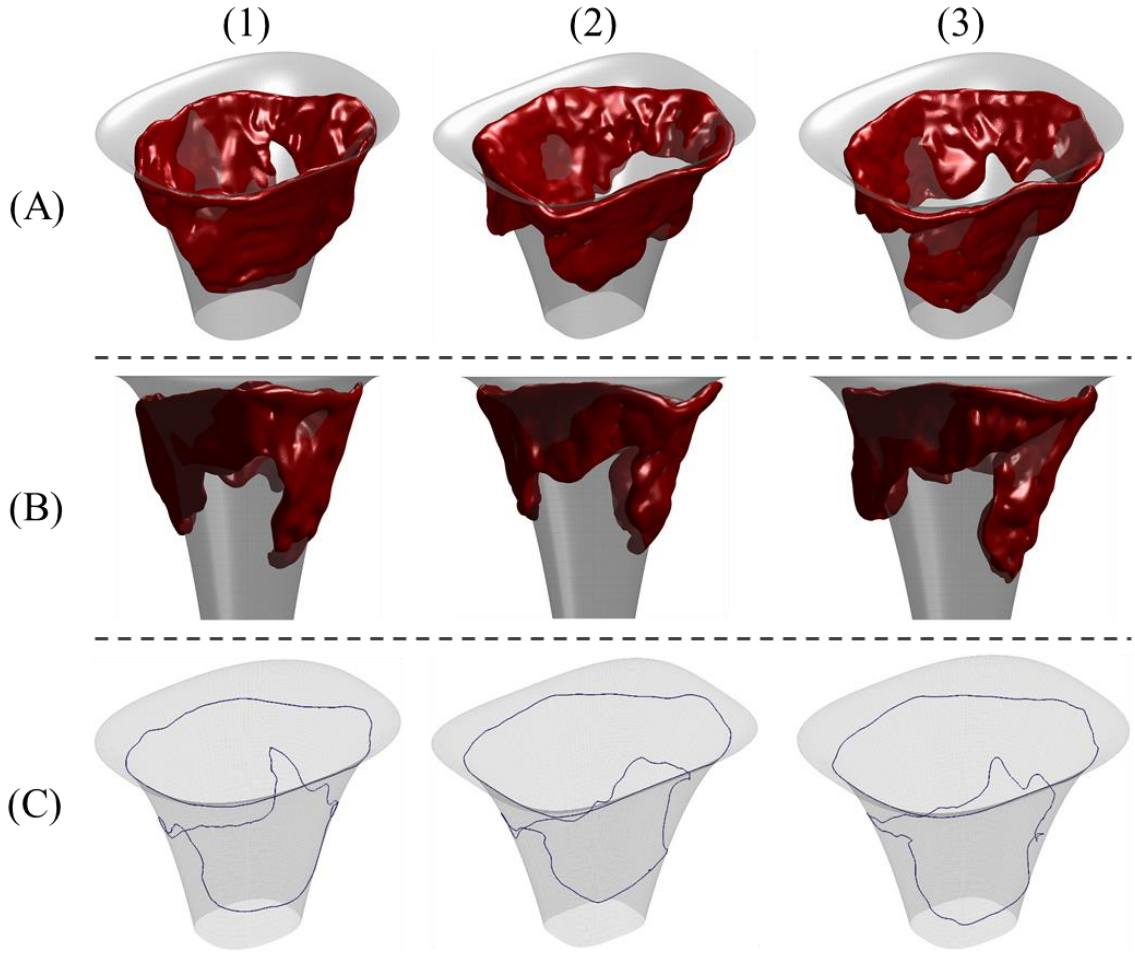

Figure 32 Computed superquadrics for three MVs are shown from two views in the Panels (A) and (B). For all the valves, the computed superquadric models are relatively similar and belong to the same family of superquadric shapes, shown in Panel (C).

These results indicate that using superquadrics to approximate the valve geometry has three main advantages. First, the fitting function finds the Euler angles for the MV shape and aligns the geometry with the principal directions. Second, by the optimization process, we find a global center for the superquadric model that registers the MV geometry with respect to the superquadric surface. Finally, superquadrics provide a reasonable approximation of the MV geometry that is sufficient for first-order simulations of the MV behavior.

B.2. Attribute Modeling

Our multi-resolution framework enabled us to enrich the parametric approximation of the MV geometry (superquadric model) with the MV surface features as the simplest class of MV attributes. Here, we present the results of the algorithms in our pipeline to capture the MV geometric details, perform spectral analysis, and reconstruct MV geometric models with adjustable level-of-detail.

B.2.a. MV Geometry Partitioning

We successfully applied our geometry partitioning algorithm to decompose the MV input geometry into atrial and ventricular surfaces (Figure 33). The partitioning results in two distinct meshes that represent two sides of the MV leaflet structure. Each side is then analyzed individually to fully capture the surface features of the MV geometry. Moreover, our partitioning algorithm automatically extracts curve representations for the annulus and the free edge (Figure 34).

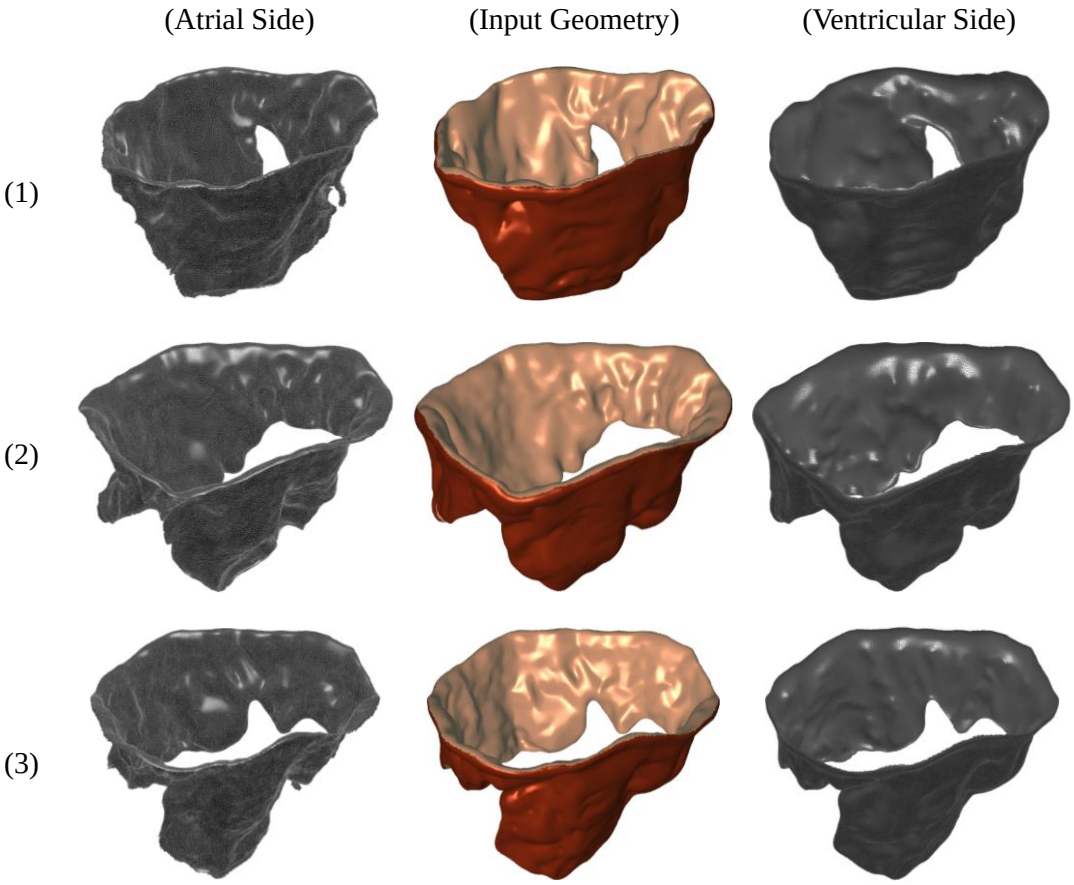

Figure 33: Mesh partitioning results to extract the atrial (beige) and ventricular (maroon) side surfaces are shown.

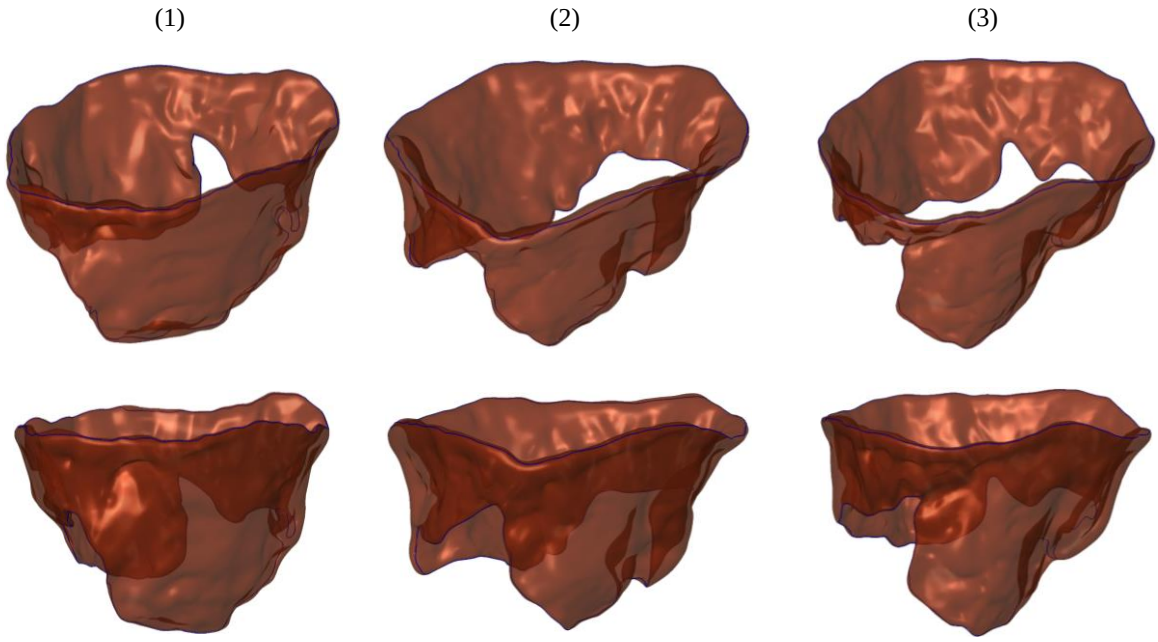

Figure 34: The annulus and free edge for 3 valves are shown as blues curves from two views. Geometrically, these curves can be sued to approximate the boundaries of the MV medial surface.

B.2.b. Spectral Analysis

Here we present our results on the reconstruction of MV geometric details by a spectral analysis method. We emphasize that modeling higher-order attributes like the fiber architecture of the leaflets can be performed using the same framework. Moreover, our methodology allows to average the geometry, geometric details, and other physical attributes of the MV leaflet structure. However, in this research document, we have focused on developing the pipeline for simplest form of attributes to present the results on the feasibility of our approach. In this section, we have shown the analysis and reconstruction results for one of the valve that we studied. The same pipeline was applied on other valves to acquire the final geometry reconstruction.

Prior to spectral analysis on the geometric details, we evaluated them by projecting the original mesh on the superquadric surface (Figure 36). In our methodology, we assumed

that the MV geometric details are regular enough so there exists a bijective projection from the input MV mesh on its superquadric fit. Otherwise, the mesh projection distorts the regions where the MV surface has folds or deviates from the superquadric model drastically (Figure 35). Thus, the geometric details in these regions cannot be reconstructed in our framework based on using superquadrics for parametrization. However, by spectral analysis, these regions are filtered out and do not distort the geometry reconstruction.

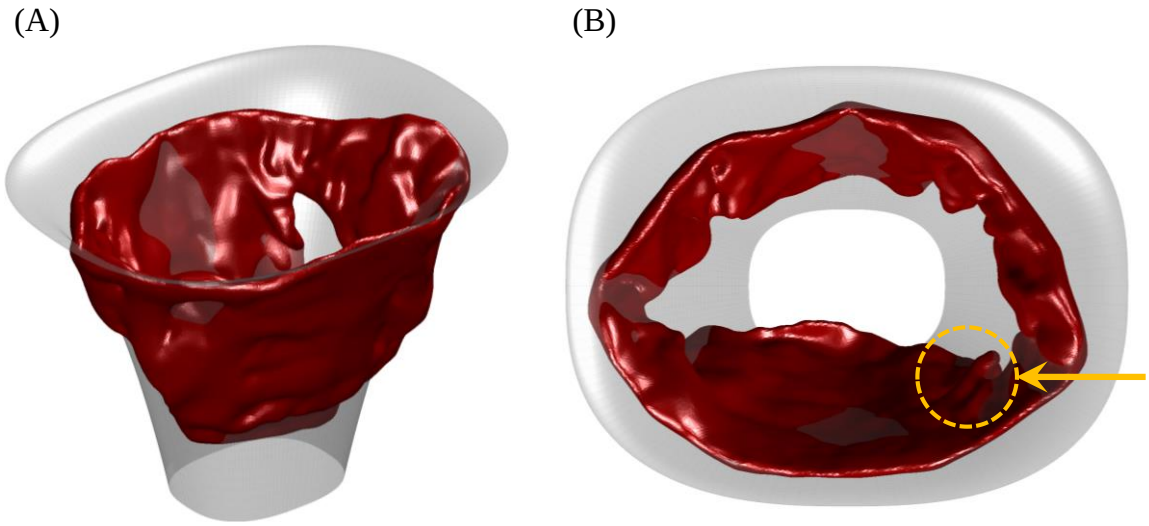

Figure 35: The regions depicted by black arrows where the valve surface has folded on itself are not recoverable by our approach. Plot (A) shows one of our studied valves that has a few folds. In Plot (B) we have shown the region that our methodology considers as high-frequency noise and filters out in the spectral analysis.

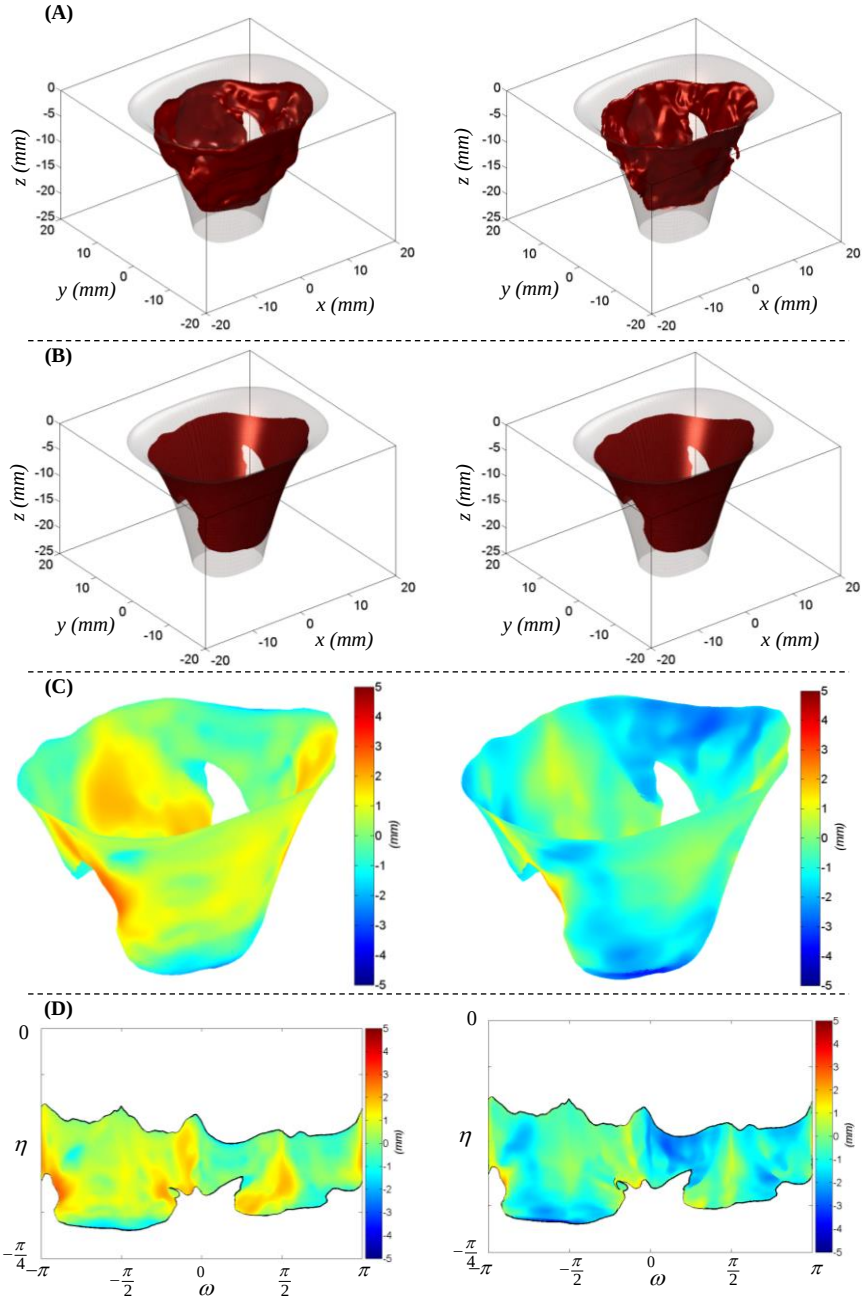

Figure 36: The two mappings required to model the geometric details of the MV leaflet is represented. The ventricular side is represented on the left and atrial on the right. The surface mesh (A) is normally projected on the superquadric fit to acquire (B). Shown in (C), the signed L_2 distance between these two meshes in (A) and (B) indicates the deviation of MV actual surface from the superquadric model. Then, the deviation fields evaluated on 3D Cartesian meshes are projected on the superquadric parametric domain as shown in (D).

We reconstructed the geometric details of the MV surface with high accuracy using spectral analysis (Figure 37). It should be noted that the spectral reconstruction recovers a scalar function on the entire periodic domain of the superquadric surface (Figure 38) that, when restricted to the MV physical boundaries, represents the MV surface geometric details (Figure 39). It can be proved that the acquired reconstruction is a unique extension of the MV geometric details to the entire parametric domain of the superquadric surface according to the Sobolev embedding theorem (Arbogast & Bona, 1999). While it is understood that the geometric details of any given valve are only defined within that valve's physical boundaries, the full field reconstruction makes it possible to average the geometry of multiple valves (having different boundaries).

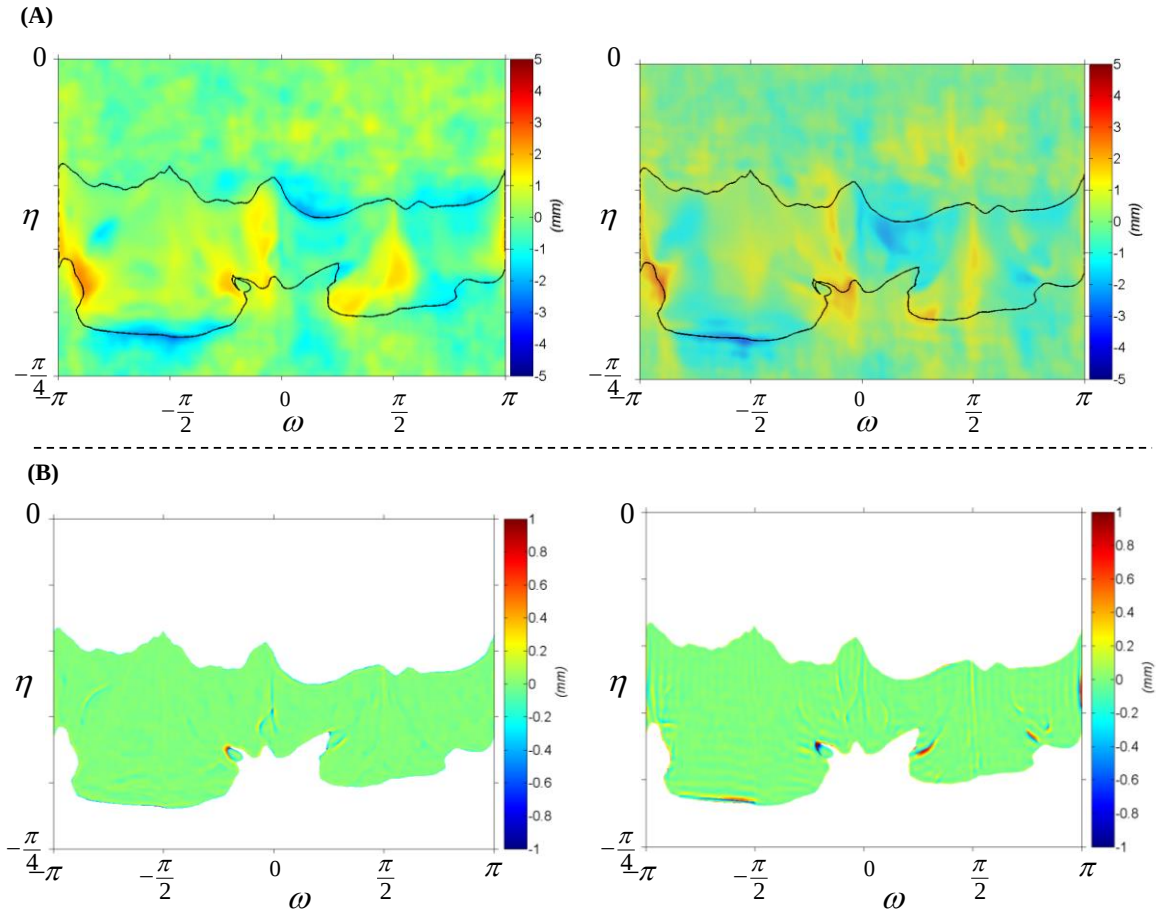

Figure 37: The reconstruction of MV geometric details for one of the studied valves, is demonstrated. Panel (A) shows the reconstruction of ventricular and atrial sides on the left and right figures respectively. The reconstruction error for both sides is illustrated in Panel (B) in the same order. It should be noted that the reconstruction error is localized in the regions where the MV surface is folded on itself.

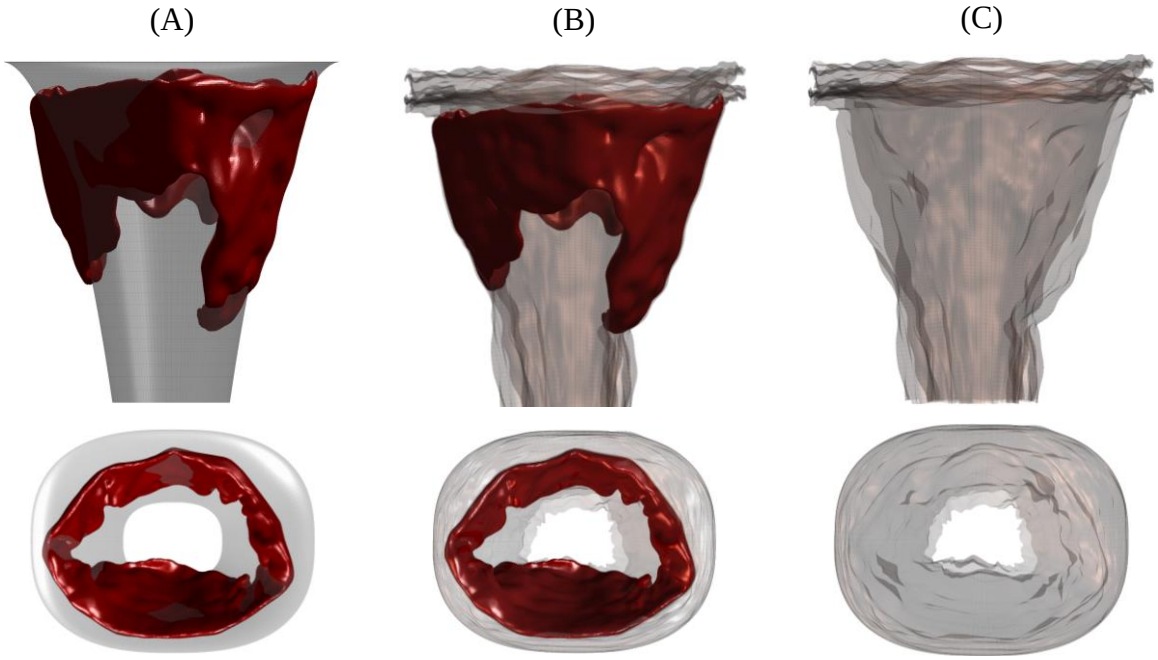

Figure 38: The reconstruction MV atrial and ventricular sides with the geometric details is illustrated. (A) shows the MV geometry input in the pipeline and its superquadric fit. In (B) the superquadric model is enriched with the geometric details to recover the fine features of the MV surface. Plot (C) shows the unique extension of the geometric details to the entire parametric domain which need to be restricted to the physical domain to recover the actual MV geometry.

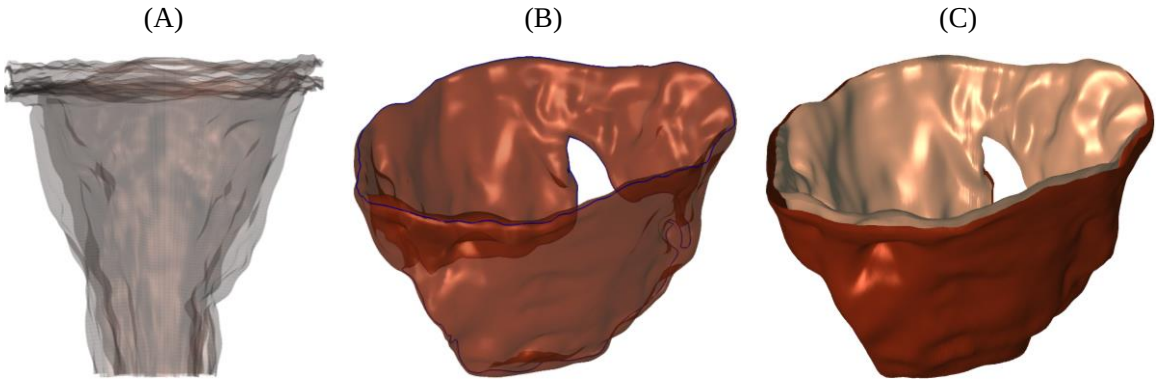

Figure 39: The spectral modeling, by definition, reconstructs the geometric details on the entire superquadric surface as shown in (A). Our parametric representation provides an explicit equation to reconstruct MV surfaces. Thus, we imposed the annulus and free edge, shown in (B) as boundaries for the parametric reconstruction. Plot (C) shows the reconstruction of MV atrial and ventricular surfaces. The result (C) shows the surfaces separate since the spectral analysis filters out the annulus and free edge regions due to their high curvature. To recover a closed representation NURBS parching can be used to stitch the two sides smoothly.

B.2.c. Multi-resolution Reconstruction

The sparse spectral analysis enabled us to characterize the geometric details of the MV in the frequency domain (Figure 40). The computed power spectrum is concentrated around the zero frequency showing that a low frequency ensemble is sufficient to reconstruct the MV geometric details with high fidelity. Furthermore, the power spectrum is fairly sparse, suggesting that a relatively small number of frequencies contain the deformation that is required to obtain the original geometry form the superquadric model. These results strongly suggest limited aliasing in the spectral analysis, which then allows filtering the MV geometric details in the spectral domain to control the level of details in the geometric model reconstruction.

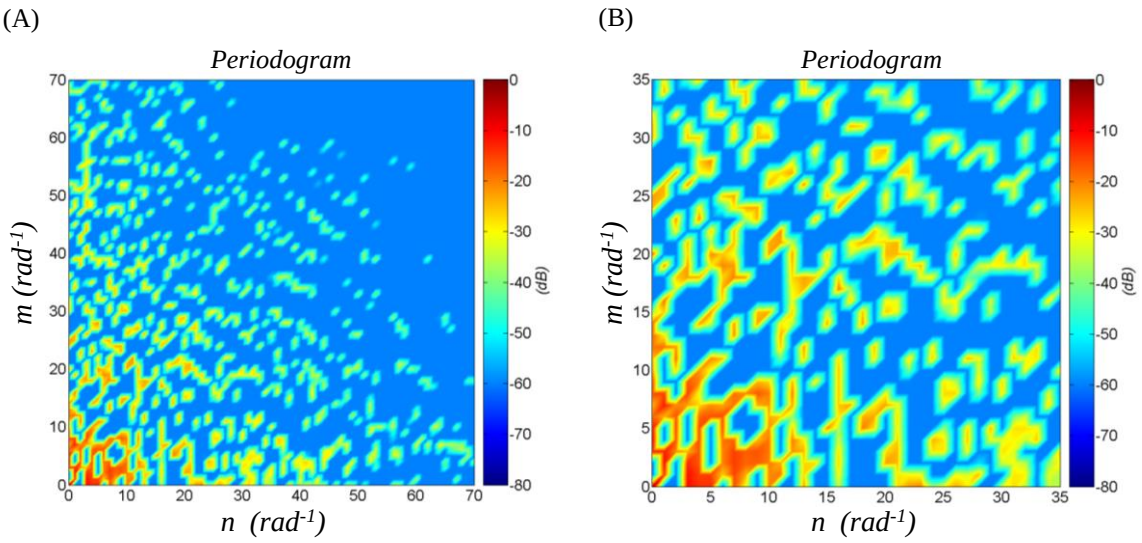

Figure 40: the spectral representation of the MV geometric details for the ventricular side for one of the studied MVs is shown in decibel. Plot (A) illustrates that the frequency spectrum is sparse and mostly concentrated at low frequencies. The horizontal axis (n) represents the frequencies along ω and the vertical axis (m) denotes the frequencies along η directions, equation (6). The low-frequency ensemble which contains more than 99% of the power spectrum density is shown in plot (B). This result indicates that we can reconstruct the MV geometric details using a relatively small number of frequencies.

The spectral modeling approach enabled us to control the level of geometric details in the final model reconstruction, which can be readily applied to other MV attributes. The results show that a superquadric surface can predict the MV general shape, which can then be enhanced to capture the surface details of the MV 3-D geometry using spectral methods. Other attributes like physical properties, multi-layered structure, or internal fiber architecture can be modeled using the same spectral approach to build attribute-rich computational models. This feature of our pipeline is extremely useful for performing finite element simulations of MV behavior since we can adjust the level of detail in the geometry as well as any other attribute reconstruction in developing computational models.

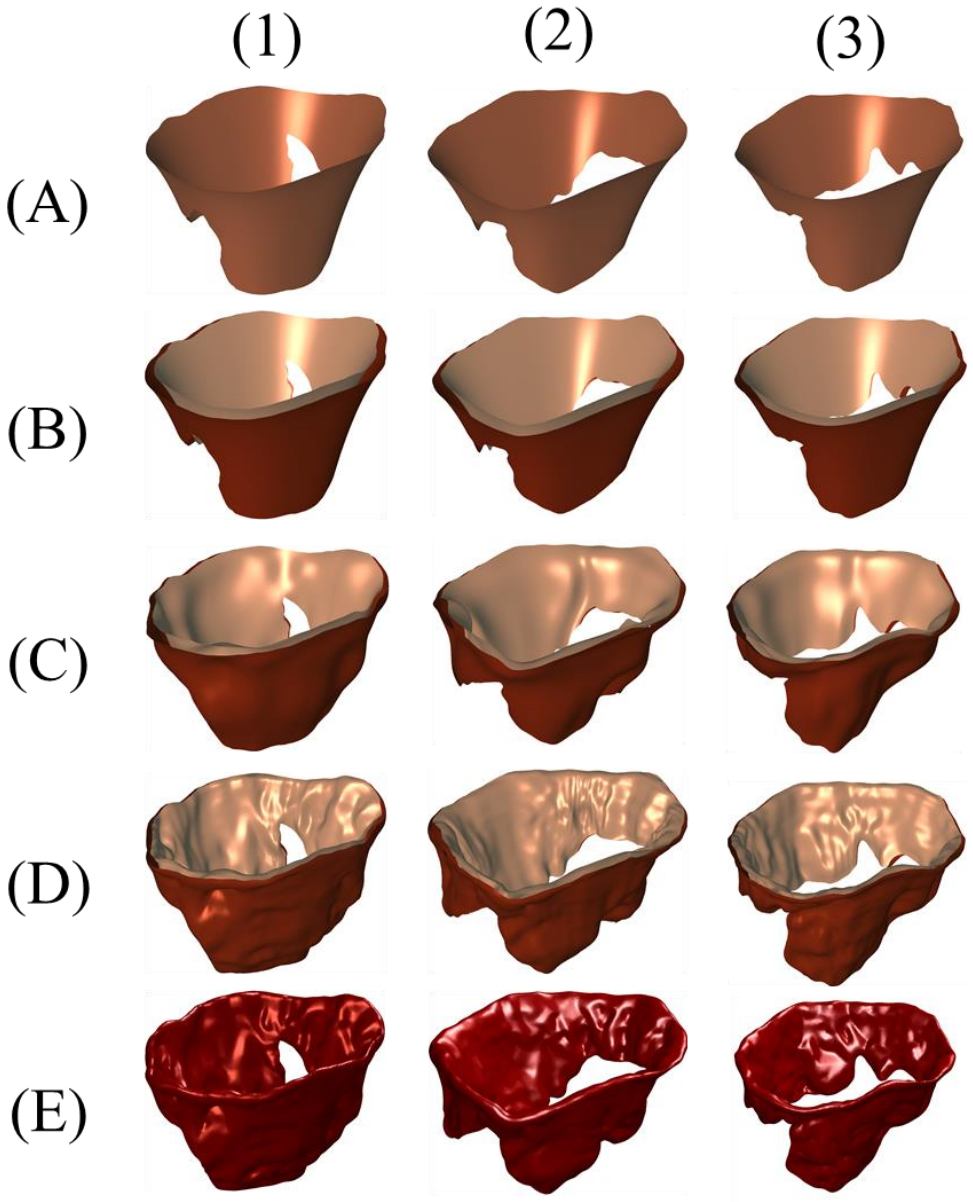

Figure 41: The results of multi-resolution reconstruction are shown for three MVs. Panel (A) shows the superquadric fits for three valves. This basic model was then morphed by adding the DC frequency to reconstruct the atrial and ventricular surfaces in (B). Integrating more frequencies in the reconstruction recovers more geometric details as shown in (C) and (D). The original geometry that is input to our pipeline is shown in (E). The hierarchical reconstruction performed by tuning the cut-off frequency in the spectral reconstruction of attributes can allow controlling the level of detail in attribute-rich model development.

B.2.d. Medial Model

Building a medial representation for the MV geometry is challenging due to the genus-1 (toroidal) topology and the multitude of physical protrusions on the surface. However, our pipeline provides a stable approach to constructing a medial representation of the MV geometry. Our approach is based on averaging the distance of the atrial and ventricular meshes from the superquadrics model. The average distance approximates the location the medial with respect to the superquadric model. This is non-trivial as our geometries are defined on unstructured meshes with different connectivity patterns (mesh topologies). In our method, spectral reconstruction establishes a correspondence between the atrial and ventricular deviation fields (Figure 42A) and enables averaging them, (Figure 42B). We also constructed the corresponding local thickness by taking the difference in location of atrial and ventricular sides, and projecting it along the normal medial surface normal, (Figure 42C).

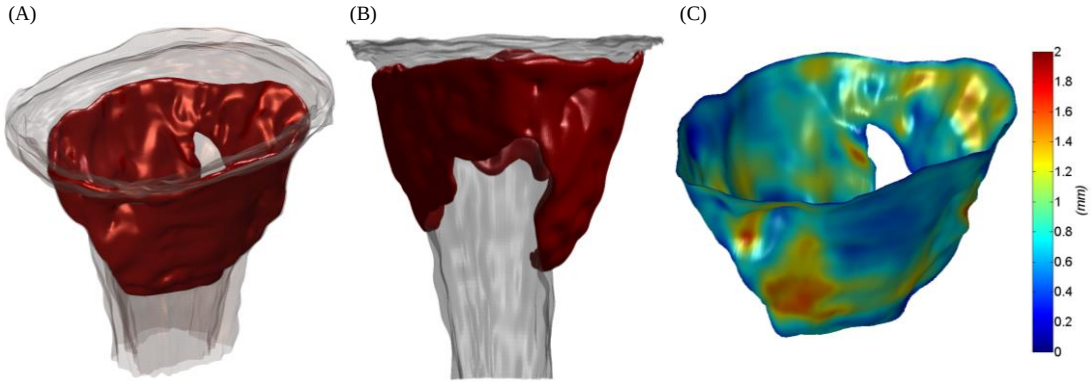

Figure 42: The medial representation of the MV leaflet structure is shown. (A) shows the reconstruction of the atrial and ventricular sides on the superquadrics parametric domain. In (B) these surfaces are averaged to acquire the location of medial surface. The complete medial representation of the MV restricted to the physical boundaries and with pointwise scalar fields is shown in (C). The thickness fields is an attribute of the MV physical structure that is essential for using shell models for finite element simulations of the MV biomechanical behavior.

Chapter 5: Discussion and Conclusions

We presented a novel approach to process medical images into a high-resolution detailed geometric models of the MV leaflet. The methodology is independent of the imaging modality and requires only a limited set of parameters to quantify the geometry of the entire MV leaflet structure. In contrast to the existing geometric models of the MV, we performed a multi-resolution analysis of the MV leaflet, with major emphasis on consistent parameterization within an objective modeling framework. This approach allows us to perform accurate quantification and reconstruction of patient-specific geometric features, and ultimately to develop a complete population-averaged geometric model of the MV. Most notably, our framework provides the basis for reconstructing MV physical attributes and incorporating them in computational models.

One of the novel features of the proposed model is the multi-resolution representation of geometry and the decoupling of general shape parameters (superquadric model) from the fine-scale features (spectral analysis). This approach is inspired by the idea of decoupling growth (volumetric changes) and adaptation/development (fine-scale tuning) of biological tissues. This decomposition ensures that quantification of inter-patient variations and development of population-averaged models unaffected by the dimensional variability between the individual MV specimens. Furthermore, by analyzing the fine-scale features in the spectral domain, we preserve the high-level of detail in the model along with the ability to adjust the level-of-detail in the reconstructed geometric model.

We firmly believe that our framework will inspire an entirely new approach to building high-fidelity computational image-based models. It is important to note the

flexibility of the proposed approach that allows for gradually increasing the level of detail of patient-specific models based on *in vivo* imaging as the imaging technologies improve. Also, our methodology can be readily applied to other heart valves, heart chambers, and many anatomical shapes to quantify and characterize their geometries. We believe that our approach provides a basis to assimilate the *in vivo* anatomically accurate information on the structure with high-resolution and attribute-rich *in vitro* models. This methodology will then lead to high-fidelity computational models for patient-specific modeling for use in surgical treatment simulations and medical device design.

APPENDIX A – micro-CT Data-sets

We imaged the valves *in vitro* to acquire high-resolution information on their shape using micro-CT, which is not feasible *in vivo.* Excising tissue from the body and working with post-mortem tissue causes untraceable changes in shape. However, we relied on micro-CT to acquire high-resolution information on the structure. Imaging MV soft tissue *in vitro* using CT imaging modality is challenging because of four main issues. First, the tissue loses moisture and the resultant change in water content disturbs the shape, which causes more deviation from the actual *in vivo* geometry. Second, micro-CT imaging is based on density variations through the structure, while the whole MV has a relatively constant density. Third, we humidified the imaging chamber to prevent the tissue from drying and chordae tendineae from clamping on itself. If the humidity of the chamber exceeds the proper range, the images will be blurry since the whole chamber content will have a density close to 1 kg/m^3. In such cases, the tissue boundary is not easy to delineate in the images. Moreover, we mounted the valves on a holder device to simulate the left ventricle of the heart (Rabbah et al., 2013). This external object will diffract the signal and blurs the tissue images. Sometimes this effect is noticeable and corrupts the 3D images. We inspected ten imaging data sets and selected five workable ones, which were least affected by the aforementioned issues.

APPENDIX B – Curvature Flow Filter

The optimal choice of filters requires an understanding of their behavior so that the quality of the image can be enhanced while the distortion can be minimized. We sought to enhance the edge contrast in images in order to segment them and delineate shape boundaries with high fidelity. Isotropic filters are insensitive toward the feature edges in an image. Therefore, we used the curvature flow filter, an anisotropic filter with adaptive performance. In this filter, the diffusion flux is directly proportional to the local curvature in the image. This adaptivity causes the high-curvature regions to diffuse more quickly than the low-curvature ones. This behavior has two advantages: First, the areas polluted by noise are characterized by predominantly high curvatures. Thus, the curvature flow filter recovers the polluted regions in an image by a higher diffusion flux that attenuates noise. Second, the image edges have lower curvatures so this filter affects them minimally. As a result, the curvature flow filter enhances the contrast resolution of the image. Furthermore, we aimed to minimize the signal dropout and loss of geometric details in the images. The curvature flow filter enabled us to control the degree to which the filter affects an image. This type of filter has two input parameters: (1) the time step, and (2) the number of iterations. The time step should be small enough to satisfy the CFL stability condition in solving the transient diffusion equation (Weickert, 1998). The time step in processing n-dimensional images needs to be less then 2^{-n}, assuming unit size of the grid. The typical value used for 3-D images is 0.0625s. The curvature-flow diffusion equation is linear with respect to time. Consequently, using smaller time steps leads to the same results while being computationally more expensive. However, because smaller time steps allow a better control over the filtering process, we used the same time step value of 0.001s in our

processing. We also chose the number of iterations empirically for each image to improve the resolution while preserving the geometric details.

APPENDIX C – Morphological Filters

We used a Dilation-Erosion filter to remove the marker artifacts from the voxel representation of each valve. The markers that we placed on the valve for shape registration distort the natural shape of the valve surface. This distortion emerges as a spurious bump map superimposed on the leaflet surface in the segmented images. An effective way to remove this bump map is by applying morphological filters. These filters are applied on the binary or gray scale images to modify the shape while accounting for the morphology of the features. We set the filter characteristics empirically to minimally disturb the geometry of the leaflet surface.

After removing the marker artifacts, we also applied a connected components filter to remove islands in the 3-D binary fields. These regions were in fact clouds of fog caused by humidifying the imaging chamber. We rectified the binary masks by applying connected a components filter, which works by clustering the voxels and then discarding the unwanted ones. We selected one of the voxels corresponding to the valve structure as a seed. Then, the voxels that were not connected to the selected seed were removed by the filter.

APPENDIX D - Superquadrics

Superquadrics are useful shape primitives as they have both implicit and explicit representations. The dual representation of superquadric shapes arises from the fact that they are the spherical product of two 2D curves (Jaklic et al., 2013). The implicit function, which is often called the inside-outside function, segments the whole 3-D space into 2 regions with respect to the superquadric surface: (1) *inside* where it's negative, and (2) *outside* where it's positive. It also provides a measure of radial distance that any point in the space has from the superquadric surface. Thus, the implicit form facilitates computing a superquadrics model of an input point cloud through minimizing the corresponding values of the implicit function. The explicit representation provides a parameterization for the superquadric surface and allows reconstructing the superquadric geometry effectively and efficiently. This form is in fact a conformal mapping from the 2D periodic domain onto the superquadrics surface. The implicit and explicit forms of the superquadric make them powerful shapes primitives and practical tools to define a basis for modeling non-standard geometries.

We used a reduced form of the superquadrics inside-outside function since the z-axis has been fixed for all the input geometries in our framework. The valves are mounted on a rigid holder, which is then positioned in a cylindrical imaging chamber. Thus, all the input image-based geometries are registered to the same z-axis *a priori*. We enforced the superquadric model that we computed to be aligned with this global z-axis by allowing the orientation to change only around z-axis. Subsequently, we used a modified inside-outside function with 9 parameters in our studies.

SUPERQUADRIC FITTING

The superquadrics inside-outside function provides an efficient way to estimate the superquadric parameters (Solina & Bajcsy, 1990). To fit a superquadrics model to an input geometry, we search for the set of parameters that defines the shape with the minimum distance from that geometry. This requires minimizing a measure of distance between the input and the model. In the least squares method, the L_2 distance between the input and the model is used as a measure of deviation:

Step 1 Make a guess for the for shape parameter set

Step 2 Project the point cloud on the shape defined by the current parameter set

Step 3 Evaluate the distance between the input point cloud and the one projected on the shape.

Step 4 If it's higher than an acceptable tolerance, update the guess; go to Step 2.

However, in most shape fittings, the projection step in the approach presented above is very costly because it is an iterative procedure by itself. The superquadrics inside-outside function, evaluated at a point, is correlated to the relative distance of that point and the superquadrics. Thus, this function provides a measure of the discrepancy between the shape of the superquadrics model and the input point cloud. Based on this fact, Soline and Bajcsy proposed an objective function to estimate the superquadrics parameter set (Solina & Bajcsy, 1990). They penalized the inside-outside function with size parameters to minimize for the dimensions while searching for the shape that follows the input geometry. However, their objective function is not entirely suitable for modeling the MV geometry, (Figure 43). Thus, we followed their approach and devised a new objective function that approximates the shape of MV.

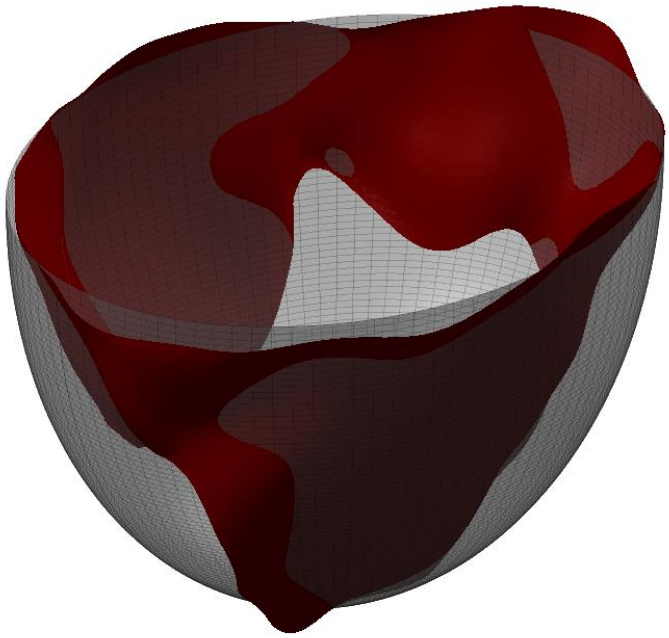

Figure 43: The standard objective function used to fit superquadric models fails to fit an acceptable model to the MV geometry. This is due to the fact that this objective function finds the closest model to the input geometry with elliptical topology. The MV geometry, however, is analogous to an hourglass shape.

APPENDIX E – Non-uniform Fourier Transform

There are a variety of NUFFT algorithms developed to perform Fourier transform on the non-evenly sampled functions (Dutt & Rokhlin, 1993), (Beylkin, 1995), (Nguyen & Liu, 1999) (Fessler & Sutton, 2003), (Potts, Steidl, & Tasche, 2001), (Feichtinger, Gr, & Strohmer, 1995). Dutt and Rokhlin (Dutt & Rokhlin, 1993) classified the NUFFT algorithms in 3 types based on the domain with non-equispaced values. The type 1 NUFFT evaluates the Fourier transform for the function values that are irregularly spaced to integral frequencies. Conversely, the type 2 NUFFT computes the function values on an irregular grid from integral frequencies. Lastly, the types 3 is the transformation from irregular samples function values to non-integral frequencies.

In our case, we wanted to evaluate the Fourier transform of fields defined on unstructured meshes to the domain of integer-valued frequencies. This is required to build a universal correspondence between the attribute fields that model the physical and structural properties of different MVs. Thus, our case is classified as a type 1 NUFFT problem. The majority of NUFFT approaches first reformulate the problem that a standard FFT computation becomes applicable (Fessler & Sutton, 2003). The appeal toward FFT is due to the algorithm's exponential convergence rate and optimal computational complexity. To reform the problem for the FFT application, many techniques interpolate the function on a regular grid. However, the interpolation step introduces approximation errors, which need to be compensated for.

One approach to cancel out the effects of interpolation is to perform NUFFT iteratively and converge to a spectrum that is not distorted by interpolation (Strohmer, 1997). The underlying assumption in this type of analysis is that the function to reconstruct is band-limited. This type of technique oversamples the function values on a Cartesian grid

and then applies a standard FFT. It is expected that the spectrum be localized on a compact support since the function is band-limited. This then leads to removing the interpolation errors through spectrum filtering since they emerge as pollution in the spectral domain. However, filtering the spectrum to remove interpolation noise also distorts the original frequency content of the function. Therefore, this procedure is repeated iteratively to incrementally remove the interpolation noise and converge toward the actual frequency content of the function.

Another approach to circumvent the interpolation artifacts is to apply interpolation kernels that can then be directly removed by convolution theorem (Greengard & Lee, 2004). The discrete function values can be reformulated as a series of delta functions multiplied by the underlying function. In this representation, the delta functions perform the sampling of the original function at scattered locations. Then, this formulation can be convolved with a kernel to interpolate the function values on a regular oversampled grid. According to the convolution theorem, the spectrum of two signals convolved in the spatial domain is the multiplication of their spectrums. Thus, applying FFT on the oversampled function results in the original spectrum of the function multiplied by the kernel's Fourier transform. The original function spectrum is then recovered by deconvolving the effect of the interpolation kernel.

Bibliography

Acker, M. A., Parides, M. K., Perrault, L. P., Moskowitz, A. J., Gelijns, A. C., Voisine, P., . . . Puskas, J. D. (2014). Mitral-valve repair versus replacement for severe ischemic mitral regurgitation. *New England Journal of Medicine, 370*(1), 23-32.

Amini, R., Eckert, C. E., Koomalsingh, K., McGarvey, J., Minakawa, M., Gorman, J. H., . . . Sacks, M. S. (2012). On the in vivo deformation of the mitral valve anterior leaflet: effects of annular geometry and referential configuration. *Ann Biomed Eng, 40*(7), 1455-1467. doi:10.1007/s10439-012-0524-5

Arbogast, T., & Bona, J. L. (1999). Methods of applied mathematics. *Department of Mathematics, University of Texas, 2008*.

Bardinet, E., Cohen, L. D., & Ayache, N. (1996). Tracking and motion analysis of the left ventricle with deformable superquadrics. *Medical image analysis, 1*(2), 129-149.

Barr, A. H. (1981). Superquadrics and angle-preserving transformations. *IEEE Comput Graph Appl, 1*(1), 11-23.

Benjamin, M. M., Smith, R. L., & Grayburn, P. A. (2014). Ischemic and Functional Mitral Regurgitation in Heart Failure: Natural History and Treatment. *Current Cardiology Reports, 16*(8), 1-11.

Berdajs, D., Lajos, P., & Turina, M. I. (2005). A new classification of the mitral papillary muscle. *Medical Science Review, 11*(1), BR18-BR21.

Bernstein, M. A., Fain, S. B., & Riederer, S. J. (2001). Effect of windowing and zero-filled reconstruction of MRI data on spatial resolution and acquisition strategy. *Journal of Magnetic Resonance Imaging, 14*(3), 270-280.

Beylkin, G. (1995). On the fast Fourier transform of functions with singularities. *Applied and Computational Harmonic Analysis, 2*(4), 363-381.

Blinn, J. F. (1978). *Simulation of wrinkled surfaces.* Paper presented at the ACM SIGGRAPH computer graphics.

Bothe, W., Miller, D. C., & Doenst, T. (2013). Sizing for mitral annuloplasty: where does science stop and voodoo begin? *The Annals of Thoracic Surgery, 95*(4), 1475-1483.

Carpentier, A., Adams, D. H., & Filsoufi, F. (2011). *Carpentier's reconstructive valve surgery*: Elsevier Health Sciences.

Carpentier, A. F., Lessana, A., Relland, J. Y., Belli, E., Mihaileanu, S., Berrebi, A. J., . . . Loulmet, D. F. (1995). The "physio-ring": an advanced concept in mitral valve annuloplasty. *Ann Thorac Surg, 60*(5), 1177-1185; discussion 1185-1176. Retrieved from http://www.ncbi.nlm.nih.gov/entrez/query.fcgi?cmd=Retrieve&db=PubMed&dopt=Citation&list_uids=8526596

Chandran, K. B. (2010). Role of Computational Simulations in Heart Valve Dynamics and Design of Valvular Prostheses. *Cardiovasc Eng Technol, 1*(1), 18-38. doi:10.1007/s13239-010-0002-x

Choi, A., Rim, Y., Mun, J. S., & Kim, H. (2014). A novel finite element-based patient-specific mitral valve repair: virtual ring annuloplasty. *Bio-medical materials and engineering, 24*(1), 341-347.
Choi, H. I., Choi, S. W., & Moon, H. P. (1997). Mathematical theory of medial axis transform. *pacific journal of mathematics, 181*(1), 57-88.
d'Arcy, J., Prendergast, B., Chambers, J., Ray, S., & Bridgewater, B. (2011). Valvular heart disease: the next cardiac epidemic. *Heart, 97*(2), 91-93.
Drach, A., Khalighi, A. H., ter Huurne, F. M., Lee, C.-H., Bloodworth, C., Pierce, E. L., . . . Sacks, M. S. (2015). Population-Averaged Geometric Model of Mitral Valve From Patient-Specific Imaging Data. *Journal of Medical Devices, 9*(3), 030952.
Dutt, A., & Rokhlin, V. (1993). Fast Fourier transforms for nonequispaced data. *SIAM Journal on Scientific computing, 14*(6), 1368-1393.
Eck, M., DeRose, T., Duchamp, T., Hoppe, H., Lounsbery, M., & Stuetzle, W. (1995). *Multiresolution analysis of arbitrary meshes.* Paper presented at the Proceedings of the 22nd annual conference on Computer graphics and interactive techniques.
Enriquez-Sarano, M., Akins, C. W., & Vahanian, A. (2009). Mitral regurgitation. *The Lancet, 373*(9672), 1382-1394.
Feichtinger, H. G., Gr, K., & Strohmer, T. (1995). Efficient numerical methods in non-uniform sampling theory. *Numerische Mathematik, 69*(4), 423-440.
Fessler, J., & Sutton, B. P. (2003). Nonuniform fast Fourier transforms using min-max interpolation. *Signal Processing, IEEE Transactions on, 51*(2), 560-574.
Flameng, W., Meuris, B., Herijgers, P., & Herregods, M.-C. (2008). Durability of mitral valve repair in Barlow disease versus fibroelastic deficiency. *The Journal of thoracic and cardiovascular surgery, 135*(2), 274-282.
Gorman III, J. H., Ryan, L. P., & Gorman, R. C. (2006). Pathophysiology of ischemic mitral insufficiency: Does repair make a difference? *Heart Failure Reviews, 11*(3), 219-229.
Gorman, J. H., 3rd, Jackson, B. M., Enomoto, Y., & Gorman, R. C. (2004). The effect of regional ischemia on mitral valve annular saddle shape. *Ann Thorac Surg, 77*(2), 544-548. Retrieved from http://www.ncbi.nlm.nih.gov/entrez/query.fcgi?cmd=Retrieve&db=PubMed&dopt=Citation&list_uids=14759435
Gottlieb, D., & Shu, C.-W. (1997). On the Gibbs phenomenon and its resolution. *Siam Review, 39*(4), 644-668.
Greengard, L., & Lee, J.-Y. (2004). Accelerating the nonuniform fast Fourier transform. *Siam Review, 46*(3), 443-454.
Hammer, P. E., Perrin, D. P., Pedro, J., & Howe, R. D. (2008). *Image-based mass-spring model of mitral valve closure for surgical planning.* Paper presented at the Medical Imaging.
Jaklic, A., Leonardis, A., & Solina, F. (2013). *Segmentation and recovery of superquadrics* (Vol. 20): Springer Science & Business Media.
Khalighi, A. H., Drach, A., ter Huurne, F. M., Lee, C.-H., Bloodworth, C., Pierce, E. L., . . . Sacks, M. S. (2015). A comprehensive framework for the characterization of

the complete mitral valve geometry for the development of a population-averaged model *Functional Imaging and Modeling of the Heart* (pp. 164-171): Springer.
Kheradvar, A., Groves, E. M., Dasi, L. P., Alavi, S. H., Tranquillo, R., Grande-Allen, K. J., . . . Goergen, C. J. (2015). Emerging Trends in Heart Valve Engineering: Part I. Solutions for Future. *Annals of Biomedical Engineering, 43*(4), 833-843.
Kunzelman, K., Cochran, R., Chuong, C., Ring, W., Verrier, E., & Eberhart, R. (1993). Finite element analysis of the mitral valve. *The Journal of Heart Valve Disease, 2*(3), 326-340.
Kunzelman, K. S., Cochran, R. P., Chuong, C., Ring, W. S., Verrier, E. D., & Eberhart, R. D. (1993). Finite element analysis of the mitral valve. *J Heart Valve Dis, 2*(3), 326-340. Retrieved from http://www.ncbi.nlm.nih.gov/entrez/query.fcgi?cmd=Retrieve&db=PubMed&dopt=Citation&list_uids=8269128
Kunzelman, K. S., Cochran, R. P., Verrier, E. D., & Eberhart, R. C. (1994). Anatomic basis for mitral valve modelling. *J Heart Valve Dis, 3*(5), 491-496. Retrieved from http://www.ncbi.nlm.nih.gov/entrez/query.fcgi?cmd=Retrieve&db=PubMed&dopt=Citation&list_uids=8000582
Lee, C. H., Zhang, W., Liao, J., Carruthers, C. A., Sacks, J. I., & Sacks, M. S. (2015). On the presence of affine fibril and fiber kinematics in the mitral valve anterior leaflet. *Biophys J, 108*(8), 2074-2087. doi:10.1016/j.bpj.2015.03.019
Lim, K. H., Yeo, J. H., & Duran, C. M. (2005). Three-dimensional asymmetrical modeling of the mitral valve: a finite element study with dynamic boundaries. *J Heart Valve Dis, 14*(3), 386-392. Retrieved from http://www.ncbi.nlm.nih.gov/entrez/query.fcgi?cmd=Retrieve&db=PubMed&dopt=Citation&list_uids=15974534
Lorensen, W. E., & Cline, H. E. (1987). *Marching cubes: A high resolution 3D surface construction algorithm.* Paper presented at the ACM siggraph computer graphics.
Lounsbery, M., DeRose, T. D., & Warren, J. (1997). Multiresolution analysis for surfaces of arbitrary topological type. *ACM Transactions on Graphics (TOG), 16*(1), 34-73.
Madesis, A., Tsakiridis, K., Zarogoulidis, P., Katsikogiannis, N., Machairiotis, N., Kougioumtzi, I., . . . Zarogoulidis, K. (2014). Review of mitral valve insufficiency: repair or replacement. *Journal of Thoracic Disease, 6*(Suppl 1), S39-S51. doi:10.3978/j.issn.2072-1439.2013.10.20
Maisano, F., Redaelli, A., Soncini, M., Votta, E., Arcobasso, L., & Alfieri, O. (2005). An annular prosthesis for the treatment of functional mitral regurgitation: Finite element model analysis of a dog bone–shaped ring prosthesis. *The Annals of Thoracic Surgery, 79*(4), 1268-1275.
Malladi, R., & Sethian, J. A. (1995). Image processing via level set curvature flow. *Proceedings of the National Academy of Sciences, 92*(15), 7046-7050.

Mangan, A. P., & Whitaker, R. T. (1999). Partitioning 3D surface meshes using watershed segmentation. *Visualization and Computer Graphics, IEEE Transactions on, 5*(4), 308-321.
Marvasti, F. (2012). *Nonuniform sampling: theory and practice*: Springer Science & Business Media.
Moré, J. J. (1978). The Levenberg-Marquardt algorithm: implementation and theory *Numerical analysis* (pp. 105-116): Springer.
Neema, P. K. (2013). The saddle shape of the mitral valve: More than just a shape. *Annals of cardiac anaesthesia, 16*(1), 1.
Nesterov, Y. (2005). Smooth minimization of non-smooth functions. *Mathematical Programming, 103*(1), 127-152.
Nguyen, N., & Liu, Q. H. (1999). The regular Fourier matrices and nonuniform fast Fourier transforms. *SIAM Journal on Scientific computing, 21*(1), 283-293.
Parikh, N., & Boyd, S. (2013). Proximal algorithms. *Foundations and Trends in optimization, 1*(3), 123-231.
Pedrazzini, G. B., Faletra, F., Vassalli, G., Demertzis, S., & Moccetti, T. (2010). Mitral regurgitation. *Swiss Med Wkly, 140*(3-4), 36-43.
Pierce, E. L., Bloodworth IV, C. H., Naran, A., Easley, T. F., Jensen, M. O., & Yoganathan, A. P. (2015). Novel Method to Track Soft Tissue Deformation by Micro-Computed Tomography: Application to the Mitral Valve. *Annals of Biomedical Engineering*, 1-9.
Potts, D., Steidl, G., & Tasche, M. (2001). Fast Fourier transforms for nonequispaced data: A tutorial *Modern sampling theory* (pp. 247-270): Springer.
Pouch, A. M., Xu, C., Yushkevich, P. A., Jassar, A. S., Vergnat, M., Gorman, J. H., . . . Jackson, B. M. (2012). Semi-automated mitral valve morphometry and computational stress analysis using 3D ultrasound. *Journal of Biomechanics, 45*(5), 903-907.
Pouch, A. M., Yushkevich, P. A., Jackson, B. M., Jassar, A. S., Vergnat, M., Gorman, J. H., . . . Sehgal, C. M. (2012). Development of a semi-automated method for mitral valve modeling with medial axis representation using 3D ultrasound. *Medical Physics, 39*(2), 933-950.
Prot, V., Haaverstad, R., & Skallerud, B. (2009). Finite element analysis of the mitral apparatus: annulus shape effect and chordal force distribution. *Biomechanics and Modeling in Mechanobiology, 8*(1), 43-55.
Prot, V., Haaverstad, R., & Skallerud, B. (2009). Finite element analysis of the mitral apparatus: annulus shape effect and chordal force distribution. *Biomech Model Mechanobiol, 8*(1), 43-55. doi:10.1007/s10237-007-0116-8
Prot, V., & Skallerud, B. (2009). Nonlinear solid finite element analysis of mitral valves with heterogeneous leaflet layers. *Comput Mech, 43*(3), 353-368. doi:10.1007/s00466-008-0310-2
Prot, V., Skallerud, B., Sommer, G., & Holzapfel, G. A. (2010). On modelling and analysis of healthy and pathological human mitral valves: two case studies.

Journal of the Mechanical Behavior of Biomedical Materials, 3(2), 167-177. doi:10.1016/j.jmbbm.2009.05.004

Rabbah, J.-P., Saikrishnan, N., & Yoganathan, A. P. (2013). A novel left heart simulator for the multi-modality characterization of native mitral valve geometry and fluid mechanics. *Ann Biomed Eng, 41*(2), 305-315. doi:10.1007/s10439-012-0651-z

Sacks, M. S., Smith, D. B., & Hiester, E. D. (1997). A small angle light scattering device for planar connective tissue microstructural analysis. *Ann Biomed Eng, 25*(4), 678-689.

Salgo, I. S., Gorman, J. H., 3rd, Gorman, R. C., Jackson, B. M., Bowen, F. W., Plappert, T., . . . Edmunds, L. H., Jr. (2002). Effect of annular shape on leaflet curvature in reducing mitral leaflet stress. *Circulation, 106*(6), 711-717. Retrieved from http://www.ncbi.nlm.nih.gov/entrez/query.fcgi?cmd=Retrieve&db=PubMed&dopt=Citation&list_uids=12163432

Schueler, R., Momcilovic, D., Weber, M., Welz, A., Werner, N., Mueller, C., . . . Hammerstingl, C. (2014). Acute Changes of Mitral Valve Geometry During Interventional Edge-to-Edge Repair With the MitraClip System Are Associated With Midterm Outcomes in Patients With Functional Valve Disease Preliminary Results From a Prospective Single-Center Study. *Circulation: Cardiovascular Interventions, 7*(3), 390-399.

Sezgin, M. (2004). Survey over image thresholding techniques and quantitative performance evaluation. *Journal of Electronic imaging, 13*(1), 146-168.

Skallerud, B., Prot, V., & Nordrum, I. S. (2011). Modeling active muscle contraction in mitral valve leaflets during systole: a first approach. *Biomech Model Mechanobiol, 10*(1), 11-26. doi:10.1007/s10237-010-0215-9

Solina, F., & Bajcsy, R. (1990). Recovery of parametric models from range images: The case for superquadrics with global deformations. *Pattern Analysis and Machine Intelligence, IEEE Transactions on, 12*(2), 131-147.

Stevanella, M., Maffessanti, F., Conti, C. A., Votta, E., Arnoldi, A., Lombardi, M., . . . Redaelli, A. (2011). Mitral valve patient-specific finite element modeling from cardiac MRI: application to an annuloplasty procedure. *Cardiovas Eng Tech, 2*(2), 66-76.

Strohmer, T. (1997). Computationally attractive reconstruction of bandlimited images from irregular samples. *Image Processing, IEEE Transactions on, 6*(4), 540-548.

Sutton, M. S. J., & Weyman, A. E. (2002). Mitral valve prolapse prevalence and complications an ongoing dialogue. *Circulation, 106*(11), 1305-1307.

Terzopoulos, D., & Metaxas, D. (1990). *Dynamic 3D models with local and global deformations: Deformable superquadrics.* Paper presented at the Computer Vision, 1990. Proceedings, Third International Conference on.

Tibshirani, R. (1996). Regression shrinkage and selection via the lasso. *Journal of the Royal Statistical Society. Series B (Methodological)*, 267-288.

Vergnat, M., Jassar, A. S., Jackson, B. M., Ryan, L. P., Eperjesi, T. J., Pouch, A. M., . . . Gorman, R. C. (2011). Ischemic mitral regurgitation: a quantitative three-

dimensional echocardiographic analysis. *The Annals of Thoracic Surgery, 91*(1), 157-164. doi:10.1016/j.athoracsur.2010.09.078

Vesely, I., & Boughner, D. (1989). Analysis of the bending behaviour of porcine xenograft leaflets and of neutral aortic valve material: bending stiffness, neutral axis and shear measurements. *J Biomech, 22*(6-7), 655-671. Retrieved from http://www.ncbi.nlm.nih.gov/entrez/query.fcgi?cmd=Retrieve&db=PubMed&dopt=Citation&list_uids=2509479

Votta, E., Caiani, E., Veronesi, F., Soncini, M., Montevecchi, F. M., & Redaelli, A. (2008). Mitral valve finite-element modelling from ultrasound data: a pilot study for a new approach to understand mitral function and clinical scenarios. *Philos Transact A Math Phys Eng Sci, 366*(1879), 3411-3434. doi:10.1098/rsta.2008.0095

Wang, Q., & Sun, W. (2013). Finite Element Modeling of Mitral Valve Dynamic Deformation Using Patient-Specific Multi-Slices Computed Tomography Scans. *Ann Biomed Eng, 41*(1), 142-153. doi:10.1007/s10439-012-0620-6

Weickert, J. (1998). *Anisotropic diffusion in image processing* (Vol. 1): Teubner Stuttgart.

Witschey, W. R., Pouch, A. M., McGarvey, J. R., Ikeuchi, K., Contijoch, F., Levack, M. M., . . . Gorman, R. C. (2014). Three-dimensional ultrasound-derived physical mitral valve modeling. *The Annals of Thoracic Surgery, 98*(2), 691-694.

You, Y.-L., Xu, W., Tannenbaum, A., & Kaveh, M. (1996). Behavioral analysis of anisotropic diffusion in image processing. *Image Processing, IEEE Transactions on, 5*(11), 1539-1553.

Yuan, Y.-x. (2000). *A review of trust region algorithms for optimization.* Paper presented at the ICIAM.